Title
Mode-Free Radiating Electromagnetic Bandgap Materials and Their Applications to Microstrip Phased Arrays

Author
Adas, Enver

Publication Date
2016

UNIVERSITY OF CALIFORNIA,
IRVINE

Mode-Free Radiating Electromagnetic Bandgap Materials and Their Applications to Microstrip Phased Arrays

DISSERTATION

Submitted in partial satisfaction of the requirements for the degree of

DOCTOR OF PHILOSOPHY

in Electrical and Computer Engineering

by

Enver Adas

Dissertation Committee:
Professor Franco De Flaviis, Chair
Professor Nicolaos G. Alexopoulos
Professor Ozdal Boyraz

2016

TABLE OF CONTENTS

LIST OF FIGURES

LIST OF TABLES

ACKNOWLEDGMENTS

I would like to thank my advisor, Professor Franco De Flaviis, for his patience and guidance. More importantly, he helped me to improve my research skills and understand the value of communication and collaboration in academic research. I would like to thank Professor Nicolaos G. Alexopoulos for his review and critical suggestions, and Professor Ozdal Boyraz for being available in my dissertation committee. Lastly, I would like to appreciate all of those who contributed to my graduate studies here at the University of California, Irvine.

CURRICULUM VITAE

Enver Adas

Education

2016	Ph.D. in Electrical Engineering and Computer Science, University of California, Irvine
2011	M.S. in Electrical Engineering, University of California, Irvine.
2009-2016	Graduate Researcher, University of California, Irvine
2007	B.S. in Electronics and Communications Engineering, Yildiz Technical University, Istanbul, Turkey

Publications

E. Adas, F. De Flaviis, and N. G. Alexopoulos," Integrated Microstrip Antennas and Phased Arrays with Mode-Free Electromagnetic Bandgap Materials for Scan Blindness Elimination," Electromagnetics, vol. 37, no. 1, 2017.

E. Adas, F. De Flaviis, and N. G. Alexopoulos," Mode-Free Electromagnetic Bandgap Materials with Broadside Radiation," in preparation.

E. Adas, F. De Flaviis, and N. G. Alexopoulos," Scan Analysis of Finite Phased Arrays Based on Mode-Free Radiating Electromagnetic Bandgap Materials," in preparation.

E. Adas, F. De Flaviis, and N. G. Alexopoulos," Integrated Antennas and Phased Arrays with Mode-Free Electromagnetic Bandgap Materials," Patent Pending.

ABSTRACT OF THE DISSERTATION

Mode-Free Radiating Electromagnetic Bandgap Materials and Their Applications to Microstrip Phased Arrays

by

Enver Adas

Doctor of Philosophy in Electrical and Computer Engineering

University of California, Irvine, 2016

Professor Franco De Flaviis, Chair

In addition to radiation, microstrip phased arrays excite substrate waves. These substrate waves are not desired since they keep energy, in the substrate, that is supposed to be radiated. Thus, array elements couple to each other through the substrate waves, and eventually radiation performance of the array degrades. Depending on the elements' excitation phase, or along certain radiation directions, almost all of the power at the array input couples to the substrate waves and radiating array fails to function as a radiator, instead it behaves as a guiding structure; this phenomenon is known as scan blindness, and it must be solved for an array to function properly.

Electromagnetic bandgap (EBG) materials are engineered composite materials and capable to forbid wave propagation at frequencies within their bandgap. This thesis is focused on the integration of EBG materials and microstrip phased arrays. To be more specific, a multifunctional structure, which can be considered as a bandgap material, an antenna element, or a phased array consisted of the elements of the proposed structure, has been designed, fabricated, and measured. Numerical eigenmode and two port transmission methods are used for the bandgap investigation. Radiation properties of the structure has been improved using an impedance matching network. Scan analyses of both infinite and finite arrays have been studied. A prototype of 3 elements linear phased array of the proposed multifunctional structure has been fabricated and its active element pattern has been measured.

The proposed multifunctional bandgap-antenna structure suppresses both bound and radiating substrate waves. Therefore, it provides complete elimination of scan blindness along all directions. In addition, unit element of the multifunctional structure has similar radiation characteristics, such as radiation pattern, gain, and polarization, as a conventional microstrip antenna; whereas, its scan behavior is the key achievement over the conventional microstrip arrays. Different from conventional arrays, this structure does not support any mode propagating along the lateral directions in the array structure; therefore, power entering to the array structure will radiate to free space.

Chapter 1

Introduction

Microstrip phased arrays have been evolving in different applications since their advent in the 1970s [1]. Their unique properties make them indispensable parts of majority of wireless communication systems. However, their widespread applications have not being able to take the full advantage of this powerful technology, primarily due to a fundamental problem of substrate waves. Upon excitation of a phased array system, in addition to steerable radiation sent to the desired direction, substrate waves are also being excited and propagate within the array structure and couple array elements to each other. Mutual coupling and scan blindness are well known classic problems attributed to substrate waves in microstrip arrays. For reliable operating of microstrip arrays, substrate waves must be eliminated. Electromagnetic bandgap (EBG) materials are known for their properties of suppressing waves in frequency bands corresponding to their bandgap regions [2]. Therefore, EBG materials can be implemented to accomplish substrate wave elimination from microstrip phased arrays.

1.1 Phased Arrays

Phased arrays consist of multiple antenna elements in order to form a directional radiation pattern which can be pointed into different directions by means of phase change at the input of the array elements. Element input amplitudes can also be altered for more sophisticated beam patterns. Phased arrays offer some unique capabilities to the wireless communication systems, such as behaving like a spatial filter, which emits or receives radiation coming from or pointing to specific directions, changing main beam radiation direction and its shape, enhancing gain of transmitter and sensitivity of receiver types antenna systems and so enabling long-range communications. Another forms of arrays, known as adaptive or smart arrays, can adapt their beam directions and shapes dynamically, by manipulating element phases and amplitudes, to avoid from interfering signals while sustaining communication link with a specified point.

Phased arrays have been using into numerous applications. The first and well known phased array application is military based radar systems. In fact, electronically controlled phased arrays were first tested on those systems in the 1950s [3]; since then the technology was applied to build a scientific instrument, radio telescope, which was used to observe the first pulsar [4]. Not only being utilized on high-tech deep space exploration machines and being inevitable part of satellites communication systems, nowadays the phased array technology is so ubiquitous that it becomes part of our daily life; we use it more often through our mobile phones and other wireless links where antenna array systems are deployed on the base stations or other forms of wireless nodes. More recently, developments in the IC technologies for RF components integration open the door for phased arrays into further mm-wave applications, such as short-range communication systems and automotive collision avoidance radars [5-6]. It also finds applications in biomedical domain for early stage diagnostics [7]. Providing communication link between mobile platforms, such as aircraft, cars, and ships, and ground or satellite based terminal points has futuristic potentials of phased arrays as well.

Among various types of array elements, microstrip antennas are the most convenient ones for most of commercial applications; mainly due to their low profile, ease of fabrication, cost effectiveness, light weight, their conformal nature, and integrable with microwave circuits. Microstrip phased arrays are more applicable to mobile based wireless communication systems. Technological improvements enhance their applications further, such as replacing satellite dish antennas and using in radar systems. However, microstrip phased arrays are suffered from substrate waves as will be detailed more.

1.1.1 Directional Radiation

Radiation pattern of individual antenna elements is determined by their geometrical shape and material composition, and mostly it is not directional but occupies a large angular space surrounding the antenna element; therefore, percentage of the radiated power to a specific direction is too low.

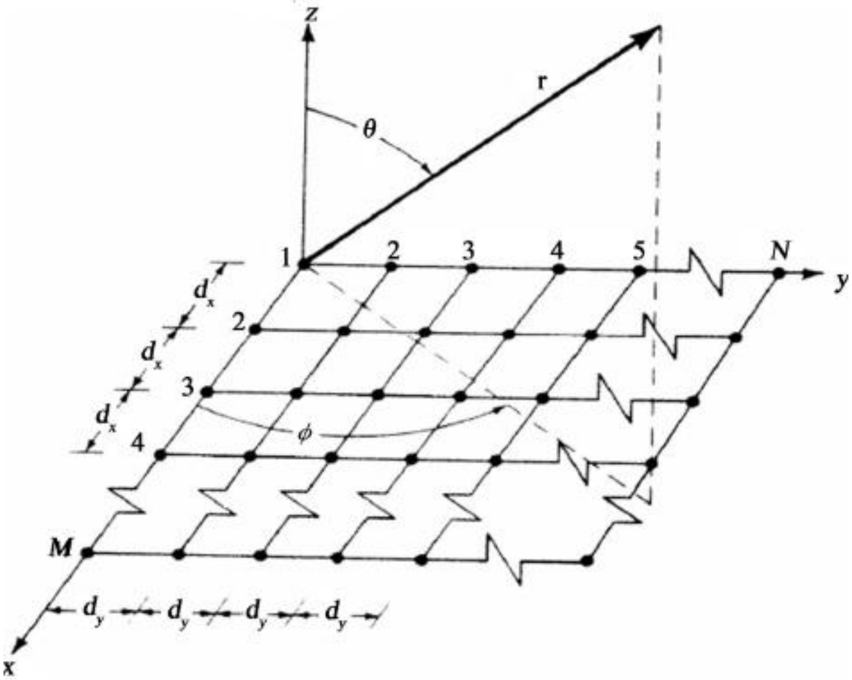

Figure 1.1 Planar phased array configuration [8].

In a two-point wireless communication link, the power received by one end of the communication link is

$$P_r = P_t + G_t + G_r + 20\log_{10}\left(\frac{\lambda}{4\pi R}\right) \tag{1.1}$$

where P_t, G_t , G_r, λ, and R are transmitted power, gain of the transmitted antenna systems, gain of the received antenna systems, operating wavelength, and distance between the transmitter and receiver respectively. In (1.1) receiver and transmitter gains vary significantly with number of antenna elements, therefore a reliable communication can be attained if number of elements is increased. However, antenna placement in an array must end up with certain configurations, as shown in Figure 1.1, in order to provide directional radiation toward the transmitter. This can be elaborated more through the concept of the array factor which will show the effect of phased arraying on the radiation pattern.

$$AF(\vartheta,\varphi) = \sum_{m=1}^{M}\sum_{n=1}^{N} A_{mn} e^{jk_0[(m-1)d_x \sin(\vartheta)\cos(\varphi)+(n-1)d_y \sin(\vartheta)\cos(\varphi)]} \tag{1.2}$$

$$AF(\vartheta,\varphi) = \sum_{m=1}^{M}\sum_{n=1}^{N} e^{jk_0[(m-1)d_x\Psi_x+(n-1)d_y\Psi_y]} \tag{1.3a}$$

$$\Psi_x = \sin(\vartheta)\cos(\varphi) - \sin(\vartheta_0)\cos(\varphi_0) \tag{1.3b}$$

$$\Psi_y = \sin(\vartheta)\sin(\varphi) - \sin(\vartheta_0)\sin(\varphi_0) \tag{1.3c}$$

$$R_a(\vartheta,\varphi) = R_e(\vartheta,\varphi)AF(\vartheta,\varphi) \tag{1.4}$$

Considering Figure 1.1, element (1,1) is chosen as a reference where its excitation phase is 0°, and all the other elements, represented by (m, n), have progressive phase shift to have directional radiation. A_{mn} in (1.2) represents complex excitation for the corresponding elements; since we are interested in changing the radiation direction only but not to obtain prescribed beam shapes or nulling, we can consider that all excitation amplitudes are unity and thus, instead of (1.2), (1.3) will be used as array factor.

Radiation coming onto the array structure from (ϑ, φ) direction, in the case of receiver array, can be considered as a plane wave. If all array elements are set to 0° phase shift, exponent in (1.2) becomes zero for only normal direction to the array, therefore beam steering cannot be performed. However, if element phases are changed, exponent of (1.3) can be zero at any direction so that radiation can be steered into different directions. (ϑ_0, φ_0) and (ϑ, φ) represent desired beam steering and actual radiation directions, respectively. Whenever $\Psi_x = \Psi_y = 0$ condition is satisfied, radiation peak will point toward (ϑ_0, φ_0) direction as shown in Figure 1.2, where the overall radiation is combination of array factor and element pattern as described by (1.4); instead of isolated element pattern, active element pattern should be used for more accurate results such as to capture substrate waves effect.

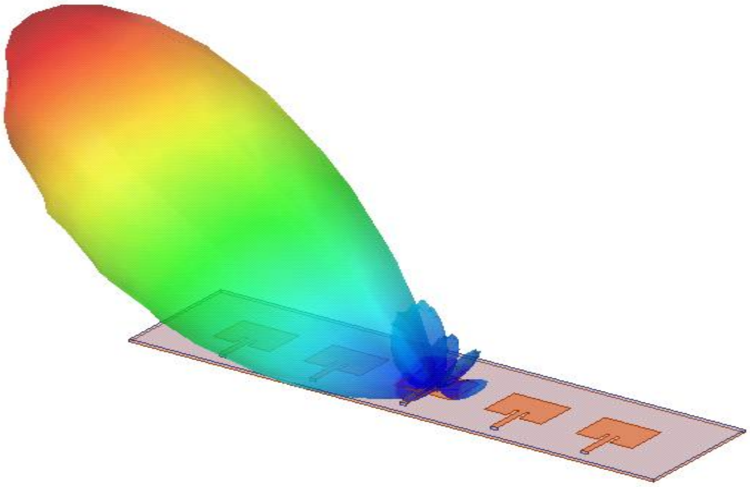

Figure 1.2 Beam steering demonstration for a phased array.

1.1.2 Grating Lobes or Floquet Modes

Exponent in (1.3) determines the pointing direction of beam maximum; if it is zero, beam maximum will point along the scan angle $\left(\vartheta_0, \varphi_0\right)$. However, its integer multiplications of 2π will also produce beam maximums, which are known as grating lobes. These secondary radiation lobes are undesired since they point along different directions from the desired scan angle, and they are strongly dependent on the element spacing, d_x and d_y, and scan angle. To make sure that grating lobes are out of visible scan ranges, element spacing must be 0.5λ or smaller along both the x- and y- directions.

In theory there are infinite numbers of grating lobes, which can be considered as Floquet modes as well. Practically only few of them are excited, while some of those excited modes couple to free space as radiation, others propagate on the array surface but are evanescent in free space. A detailed examination of both radiating and evanescent grating lobe modes is crucial since the radiating modes reduce main beam efficiency and the evanescent modes can couple to surface waves and induce mutual coupling and scan blindness in microstrip arrays. In order to analyze their propagation in the array structure, each of them can be decomposed in its x- and y- components and represented by indices $\left(p, q\right)$. Using array periodicity and (1.3), the wavenumber components of the Floquet modes in the array structure becomes

$$k_{xp} = k_0 \sin(\vartheta)\cos(\varphi) = p\frac{2\pi}{d_x} + k_0 \sin(\vartheta_0)\cos(\varphi_0) \tag{1.5a}$$

$$k_{yq} = k_0 \sin(\vartheta)\sin(\varphi) = q\frac{2\pi}{d_y} + k_0 \sin(\vartheta_0)\sin(\varphi_0) \tag{1.5b}$$

Note that (1.5) can be applied to both radiating and evanescent grating lobe modes. (p,q) = $(0,0)$ Mode corresponds to the desired main beam pointing along the scan angle (ϑ_0,φ_0), while higher order modes will radiate to the different directions or stay in the substrate as they are evanescent in free space. k_{xp} and k_{yq} will be used to determine scan blindness condition in the next section.

1.1.3 Microstrip Phased Arrays

Microstrip antenna elements are printed on grounded dielectric substrates which supports electromagnetic waves such as surface and leaky wave modes. Properties of these modes have been well studied due to their broad range of applications; dielectric constant and substrate thickness are the primary parameters defining their behaviors. A rule of thumb equation defining cut-off frequencies of surface wave modes is,

$$f_c^{(n)} = \frac{nc}{4d\sqrt{\varepsilon_r - 1}} \tag{1.6}$$

where n is mode number (even for TM modes and odd for TE modes), c is speed of light, and d is dielectric substrate thickness. Fundamental TM_0 has zero cut-off frequency therefore it is supported by very thin dielectric substrates with small dielectric constants as well.

The wave number of surface and leaky waves is represented by $k = \beta - j\alpha$, where β and α are phase and attenuation constants. As shown in Figure 1.3, surface wave modes are bounded to the dielectric substrate and decay only in the air medium, whereas leaky waves propagate both in dielectric and air mediums but decay along the x- direction due to energy leakage to the air medium.

Radiation characteristics of surface and leaky waves are given in Figure 1.3b, surface waves are types of slow waves therefore their phase constant is larger than that of the waves propagating in free space (k_0) at the same frequency. Thus, phase matching cannot be obtained for surface wave modes, $(\beta_{sw} \neq k_0 \sin(\theta))$; because of that they cannot couple to air medium as radiating waves. Leaky waves, on the other hand, are fast waves and phase matching $(\beta_{lw} = k_0 \sin(\theta))$ can be obtained for them so that they can radiate to air medium.

It is important to note that determining of phase (β) and attenuation (α) constants of these types of modes is not that straightforward for practical applications where most of the structures contain various types of materials and geometrical features. In general, numerical full wave softwares are applied to analyze these characteristics.

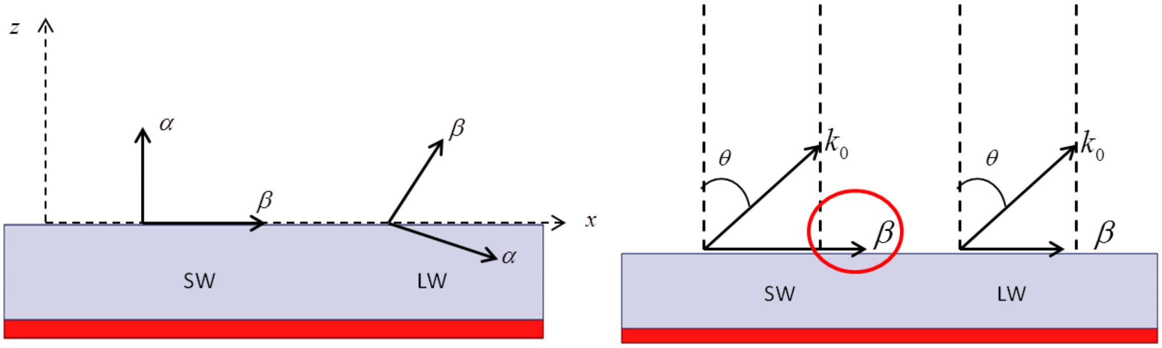

(a) (b)

Figure 1.3 (a) Propagation and (b) radiation characteristics of surface and leaky wave modes supported by grounded dielectric substrates.

Since microstrip antennas are printed on grounded dielectric substrates both surface and leaky waves discussed above are effective on their performance. Once antenna elements are excited for radiation, due to electromagnetic couplings, substrate modes are also being excited. Substrate modes excitation is more effective along certain directions depending on antenna's feeding position. Substrate modes couple energy from the antenna structures to the propagating waves in the substrate. These propagating waves couples antenna elements to each other and degrade antenna performance. From another point of view, energy coupled to the substrate waves will remain in the structure therefore overall radiation efficiency

$$e = \frac{P_{radiated}}{P_{total}} = \frac{P_{radiated}}{P_{radiated} + P_{conductor} + P_{dielectric} + P_{sw+lw}} \tag{1.7}$$

will be reduced. Where total power is split into radiated power, dielectric and conductor losses, and coupled power to the substrate modes, i.e. surface and leaky waves.

In addition to radiation efficiency reduction and mutual coupling between array elements, resonance condition known as "scan blindness" is also attributed to the substrate modes and can have dramatic effects on microstrip phased arrays. This condition occurs when phase matching between grating lobes or Floquet modes, given in (1.5), and surface or leaky wave substrate modes is satisfied,

$$\beta_{sub} = \sqrt{k_{xp}^2 + k_{yq}^2} \tag{1.8}$$

where β_{sub} can be phase constant of surface or leaky waves, depending on the effective wave type. At resonance condition or scan blindness, substrate modes are strongly excited and all of the excitation power couples to substrate modes, therefore array does not radiate. The power coupled to substrate modes will eventually returns back to the generator. Scan angles, element spacing, dielectric constant, and substrate thickness are effective parameters determining scan blindness condition; increasing any of these parameter will shift blind angle toward the broadside direction, or making scan blindness more dominant. Scan blindness is more effective on larger arrays as shown in Figure 1.4, where microstrip patch arrays are analyzed. While

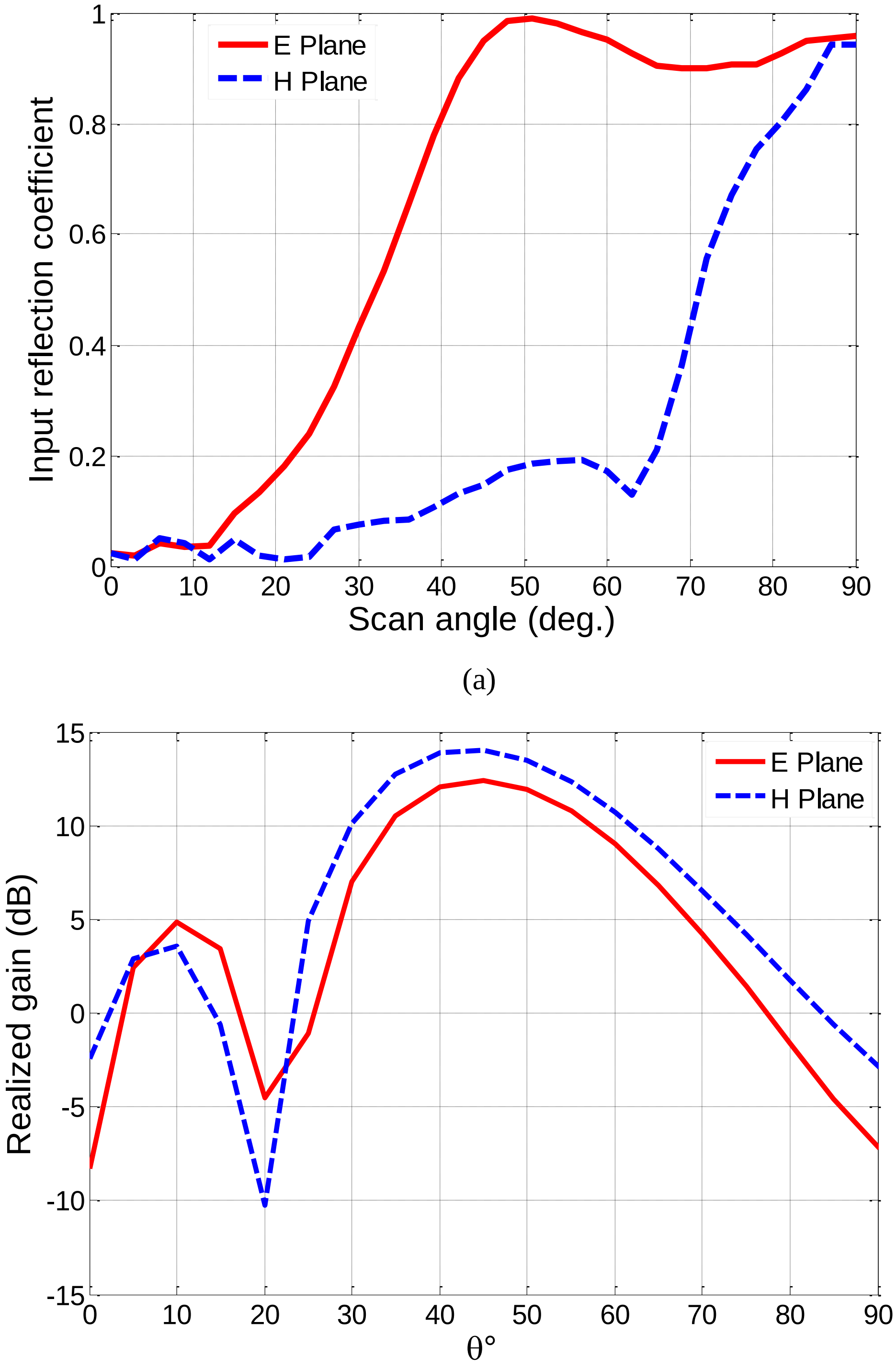

(b)

Figure 1.4 Substrate wave effect (scan blindness) on microstrip arrays. (a) Input reflection coefficient of an infinite array and (a) realized gain pattern of a 5 x 5 array for scan angle of 48°, corresponding to blindness angle.

infinite array's input reflection coefficient is much larger at E- scan plane, where blindness is effective, than H- scan plane; the difference is not that large, even though the effect of blindness is clear, in realized gain pattern of a 5 x 5 array. For larger arrays, array gain decreases substantially near blindness angle.

1.2 Electromagnetic Bandgap Materials

Electromagnetic bandgap (EBG) materials prohibit wave propagation in their structures along specified directions at frequency bands corresponding to their bandgap regions; a true electromagnetic bandgap material must be able to eliminate both surface and leaky waves. It is worth to noting that within bandgap frequencies, waves cannot propagate along horizontal directions while they can still radiate into the air medium, normal to the material structure, since normal radiation can still have horizontal or lateral wavenumber of $k_{\|} = 0$.

Figure 1.5 demonstrates bandgap characteristics of a bandgap material; where transmitted power excites substrate waves and propagates in the structure, however received power exhibits a null in its frequency response where the bandgap property of the substrate material is effective. Because of their substrate wave elimination capabilities, EBG materials have been placed between antenna elements to reduce the effect of substrate waves on antenna arrays, such as mitigating mutual coupling and scan blindness.

Bandgap property of EBG materials is not the same along all directions; indeed, a material may provide bandgap behavior in some directions while it does not show up bandgap property along the other directions. While it is sufficient to have bandgap along only one direction for EBG materials integrated with linear arrays, planar antenna arrays require EBG materials with

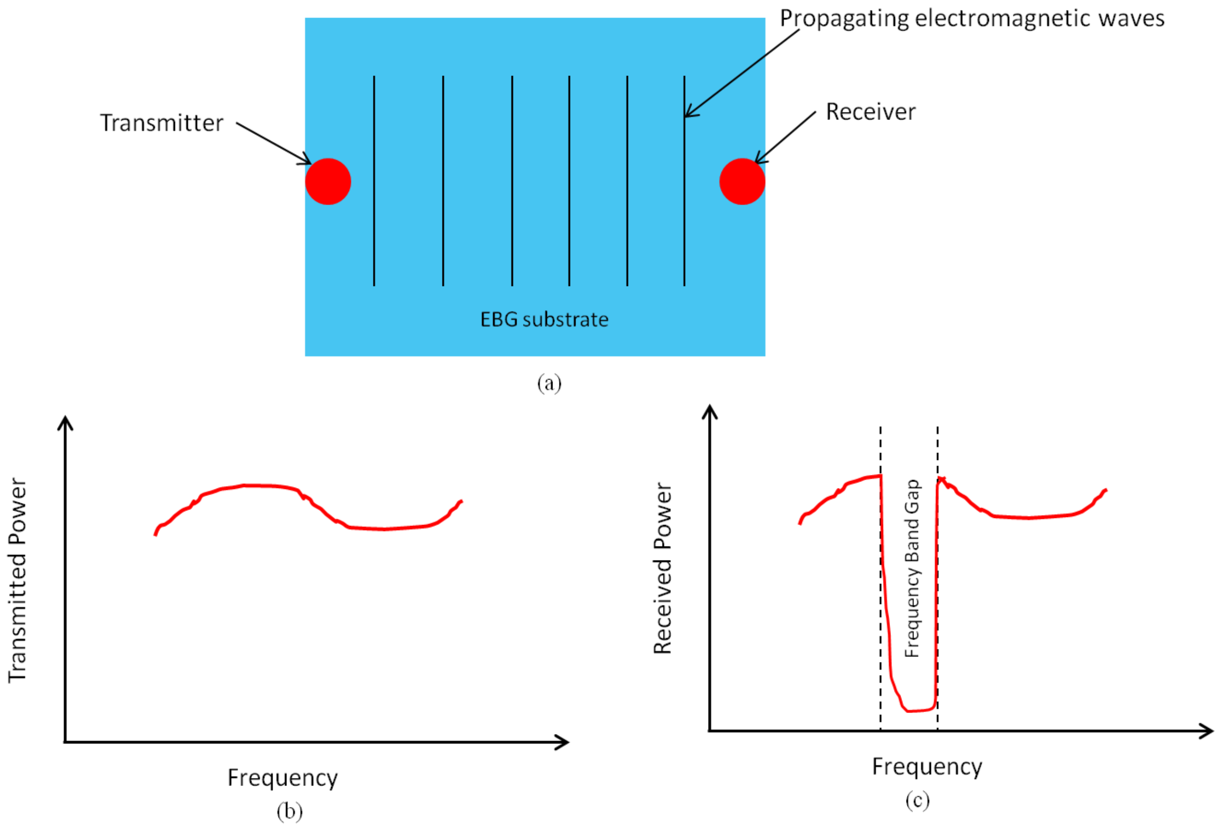

Figure 1.5 Frequency bandgap characteristic of EBG materials.

bandgap property along all horizontal directions for a complete elimination of substrate waves from the antenna arrays. Another important point of the integrated EBG materials and antenna arrays is that bandgap properties of EBG materials will be affected from the couplings between EBG and antenna metallization, therefore these couplings must be taken into account for a proper bandgap analysis of the integrated structures. EBG materials' bandgap properties are usually investigated using eigenmode and transmission setups on full wave numerical simulators, we also used such a software package, HFSS, for the bandgap characterization.

1.3 Literature Review and Challenges

Scan blindness phenomenon [9-14] is a fundamental limitation of microstrip phased arrays, and has been studied for more than three decades. Its elimination is essential to sustain communication links between wide scan angle wireless systems. Even though it is a well known problem, attributed to the coherent coupling between substrate modes and array radiation, its elimination has been remained a challenge. In fact, several different approaches were utilized to completely eliminate it or improve array scan characteristics, each of those methods has certain limitations on the array performance. These are: Subarray of elements to distort coherent coupling [15], active device with parasitic patches and shorting metallic post loaded substrates [16-17], inhomogeneous substrate [18], reduced surface wave antenna elements [19], metamaterials [20-21], defected ground structure [22-23], substrate integrated waveguide [24], and electromagnetic bandgap (EBG) materials [25-31]. Further, recently several researchers have investigated designs on increasing the scan volume of the arrays through not directly eliminating the substrate modes but modifying feeding structures or elements [32-35], using novel array elements [36], and taking advantage of the excited substrate modes [37]. Among all of these approaches, EBG materials improved the scan characteristics the most; in fact, other techniques can improve the scan range or eliminate blindness partially along only certain directions. EBG materials [2, 38-39], on the other hand, provide omnidirectional frequency bands where surface waves are eliminated along all directions; hence, they are state-of-the-art materials for the integrated phased arrays.

Integrated microstrip phased arrays and EBG materials for scan blindness elimination have been avoided from the couplings between array and bandgap metallization in order to protect performance of the isolated structures, i.e. antenna and bandgap unit elements. Bandgap materials and array elements were characterized separately first, then integrated. For example, in [27] and [29] authors placed EBG cells away from the array elements to reduce the couplings between them. EBG cells surrounded by lossy materials have also been used to suppress higher order modes due to interactions between EBG and antenna elements [31]. Microstrip dipole antenna elements, on the other hand, have been directly printed between EBG cells without devoting room to the radiating elements [26]. Element spacing of scanning arrays is half wavelength or smaller at the upper edge of the operating frequency band to have no grating lobes in the visible scan ranges. Therefore, conventional EBG techniques to remedy scan blindness with that prescribed element spacing make the surface of the integrated structure a metallic cover and degrade antenna elements radiation characteristics by using lossy materials or smaller radiating elements. A complete solution to the integrated EBG materials and planar phased arrays which remove bandgap metallization from the radiator layer so that frees antenna element size constraints, improves radiation efficiency, and using interactions between EBG and antenna elements beneficially instead of avoiding from them has remained a challenge. Artificial magnetic conductors (AMC), however, have been used properly by suppressing surface waves while physical AMC layer underneath the antenna elements and projecting AMC behavior in space to the antenna layer [40]. Projecting AMC behavior in space is a smart way to take into account artificial substrate metallization and antenna elements interactions while improving radiating system's performance. AMC structures, co-designed with the radiating elements, are good candidates for antennas [41] and broadside arrays [40]; similarly, in an another application, superstrate materials, designed as an integral part of the radiating structures, were also showed their ability to suppress surface waves from the broadside arrays [42]. For phased arrays one must ensure that the substrate wave elimination is achieved for all scan angles, therefore EBG materials will be right choice.

Surface wave effects and their suppression using EBG structures have been well studied in the context of the scan blindness; however, leaky waves, which also propagate within the printed array substrates and are potential to induce scan blindness and mutual coupling between array elements, suppression has not been investigated so far from practical microstrip phased arrays for scan blindness mitigation. A true integrated structure must offer both types of substrate waves, i.e. surface and leaky waves , elimination capabilities. Even though such modeless EBG structures have been proposed in [39], their integration with practical scanning microstrip phased arrays has not been investigated yet.

It is important to note that another class of metamaterials or bandgap materials, which radiates modes supported by their structures, as in [43-47], cannot be applied for scan blindness elimination since the radiating mode propagates in the substrate also and couples elements to each other. However, the structure presented in this thesis does not support any modes along the lateral directions, but at the same time it radiates to broadside direction while satisfying geometrical size constraints for a phased array element. Therefore, in this thesis we present a complete solution to the integration of phased arrays and electromagnetic bandgap materials.

1.4 Dissertation Outline

This thesis presents a design method for a multifunctional structure which functions as a bandgap material, with suppressing surface and leaky waves properties, and a phased array antenna element simultaneously. The presented radiating-bandgap multifunctional structure demonstrates a complete elimination of scan blindness from microstrip phased arrays.

Chapter 2 studies geometrical and modal properties of the radiating-bandgap structure. For modal analyses, eigenmode and two port transmission setups are used in order to capture characteristics of radiating modes. The geometry of the unit cell allows omnidirectional bandgap behavior.

Chapter 3 investigates the structure as an antenna element, therefore its radiation is characterized through pattern, gain, and polarization. A stripline impedance matching network is used to match its input impedance to 50 Ω.

Chapter 4 presents the effect of substrate waves on scan behaviors of microstrip phased arrays. In particular, scan blindness attributed to surface and leaky modes are detailed and the capability of the radiating-bandgap structure in elimination of scan blindness is demonstrated. In addition, couplings between metallic inclusions in a unit element of the presented structure are investigated.

Chapter 5 focuses on experimental realization of a 3 element prototype linear array based on the radiating-bandgap element; for that, the smallest possible array size is determined such that it can capture the scan blindness effect on phased arrays of the uniform substrates.

Chapter 6 summarizes the thesis and discusses the perspectives of the design methodology and the structure presented throughout this thesis.

Chapter 2

Modal Analysis of Bandgap-Antenna Element

Printed antenna arrays excite substrate wave modes, which induce mutual coupling and scan blindness in arrays. Antenna and feeding metallization affect mode properties, and should be taken into account properly. For example, a periodic patch array on a grounded dielectric substrate supports leaky waves propagating within the substrate; however, if the modal analysis omits these periodic patches, representing antenna elements, these leaky wave modes would not be captured. Thus, a complete modal investigation of the printed antenna arrays requires an antenna element as a whole structure with all types of loadings in the unit element. This is important, especially if the array substrate consists of composite structures, such as EBG or other types of metamaterial structures.

In this Chapter, we perform modal characterization of a uniform substrate microstrip patch antenna element as a reference, and the multifunctional composite bandgap-antenna structure unit element on their complete geometry and material profiles; all parts within unit cells are considered. The modal characterization techniques, i.e. eigenmode and transmission, we present here provide both bounded and radiating mode properties. Using these modal analysis techniques, the goal is to design a composite bandgap structure which eliminates both bound and radiating modes, and then use this composite structure as an antenna element for scan blindness-free phased array design. Even though the structure does not support any mode along the lateral directions, it still radiates to the direction normal to the array surface.

2.1 Unit Cell of Bandgap-Antenna Structure

Although suppressing of bound modes using conventional EBG structures has been used previously for scan blindness elimination [26-27], suppressing radiating lateral modes is also essential for printed phased arrays since these modes also couple array elements and potentially induce scan blindness. A unit element of the composite bandgap-antenna structure, which is the focus of this thesis and shown in Figure 2.1, is capable of forbidding both bound and radiating types of modes propagating laterally, along all directions within the substrate. The presented structure, thus, eliminates the scan blindness, if it used as an array element, completely from all scan directions. Another important feature of this structure is that there is no metallization pattern, other than patches serving as radiators, on the antenna layer, and all the other metallization are embedded underneath the antenna layer, whereas conventional integrated EBG and phased array structures have both radiating and bandgap metallization on the same layer [26-27, 29-31]. The bandgap is obtained from the whole structure, including antenna and embedded metallic layers; but not from the embedded metallic structure only, otherwise embedded two layers of concentric rings would not provide bandgap at frequency of interest. Size of the unit element structure is equal to the free space half-wavelength at frequency which is within the bandgap.

Detailed representation of a unit cell of the proposed multifunctional material is illustrated in Figure 2.1. The top metallic patch functions as a radiator, and the two layers of embedded rings are employed to introduce the bandgap behavior as they are considered together with the top patch as a one structure for characterizations. Rogers TMM6 $(\varepsilon_r = 6.00$, $\tan\delta = 0.0023)$ is used as the substrate material. The size of the unit cell, D, corresponds to the element spacing since we use the same unit element for both modal characterizations and antenna element of the phase arrays. The geometrical parameter values of the structure are (mm): D=50, L=23, h1=2.54, h2=3.175, h3=1.27, h=6.985, w0=2, w1=3.8, w2=3.8, w3=3, d=0.8, r1=10, r2=15, r3=20.

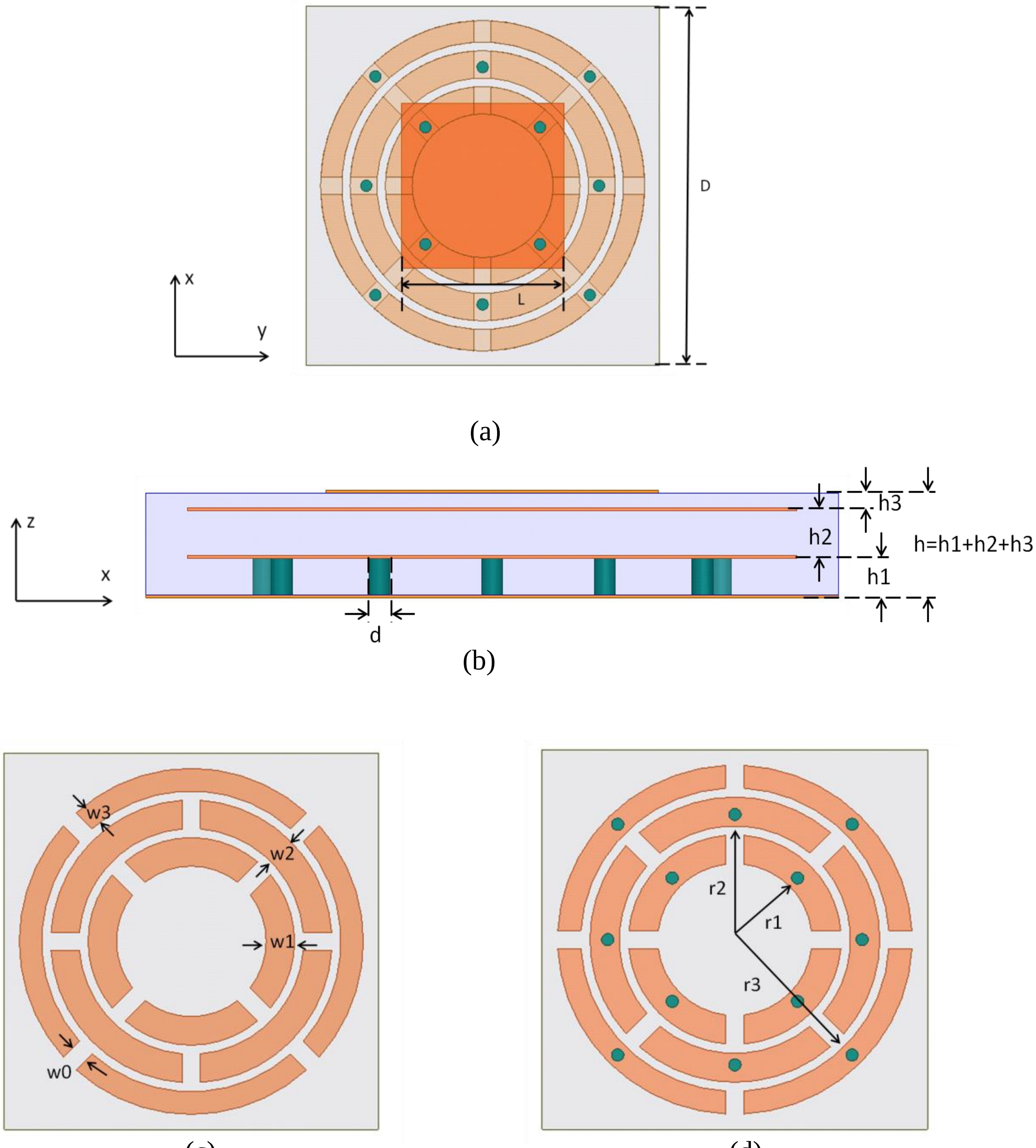

(a)

(b)

(c)

(d)

Figure 2.1 Unit cell of the multilayer multifunctional composite bandgap-antenna structure. (a) Top and (b) cross section views. Top views of (c) upper and (d) bottom (with vias) concentric rings.

We also use a microstrip patch antenna element on a uniform substrate, without any other metallization within the substrate, as a reference, to demonstrate the performance of the presented composite structure throughout this thesis. This uniform patch antenna is also square and resonates at the same frequency as the bandgap-antenna structure, within an infinite planar array environment. The width of the uniform substrate patch is W=19.5mm; element spacing, substrate material and thickness remain the same as the composite one.

An excitation probe feeds the radiating patch, and the feed position from the edge of the patch is equal to 3.5 mm and 1.75 mm for the composite and uniform unit elements, respectively. In both cases, the feeding probe is not considered for bandgap analysis since placing the probe breaks the symmetry and invalidates triangle reduced Brillouin zone and thus, omnidirectional dispersion investigation would be difficult. However, we have studied the feeding probe effect on the bandgap, along the normal axes, through different probe positions using two different characterization techniques, i.e. eigenmode and transmission; we found that its impact on the bandgap is insignificant. Therefore, in the following modal analyses, the feeding probe will not be included.

2.2 Eigenmode Analysis of Bandgap-Antenna and Uniform-Substrate Antenna Elements

The eigenmode analysis of the unit cell is performed using a commercial finite element software (Ansys HFSS). In the simulation setup, periodic boundaries are used at the sides of the unit cell and an absorbing material (PML) terminates the setup from the top. The radiating modes from the structure surface propagate within air, filled between the unit cell surface and PML, and are absorbed from the top. The solver provides eigen frequencies for given propagation phases across one unit cell.

Our approach is different from conventional EBG materials, where the unit cell size is usually smaller than $0.1\lambda_0$. Here unit cell size is about $0.5\lambda_0$. The same element will be used as a radiating element within the phased array environment where it is desired to have element spacing around $0.5\lambda_0$ for scanning purposes. λ_0 denotes free space wavelength at the phased array operating frequency or at the bandgap frequency. We aim to overlap these two frequency bands. The physical size of the unit element is 50 mm. This corresponds to $0.5\lambda_0$ at 3 GHz, i.e. the upper end of the prescribed bandgap frequency region which is from 2.90 to 3.00 GHz. We use a triangle reduced Brillouin zone since the top patch and the unit element are square. Also the rings shape and via configurations are rotationally symmetric. The structure is characterized for an omnidirectional bandgap for the prescribed frequency band mentioned above.

In order to obtain the bandgap from the dispersion diagram, both radiating and bound modes should be detected. However, the solver we use is incapable of capturing leaky wave modes properly. The modes in the leaky wave region follow the light line and merge at the frequency, corresponding to one half-wavelength which is equal to the unit element size, of 3 GHz, as shown in Figure 2.2. The bandgap region is from 3 GHz to the peak frequency of the highest bound mode below 3 GHz; the lower edge bandgap frequency can be in the other sections of the dispersion diagram, as will be explained. Thus, it is critical to understand the role of the modes following the light line above the peak frequency of the highest bound mode and merge at the maximum frequency of the dispersion analysis, which is 3 GHz here; like the modes 4 and 5 of Figure 2.2a. In fact, some of these modes are nonphysical and make it unclear whether in fact actually any frequency bandgap exists.

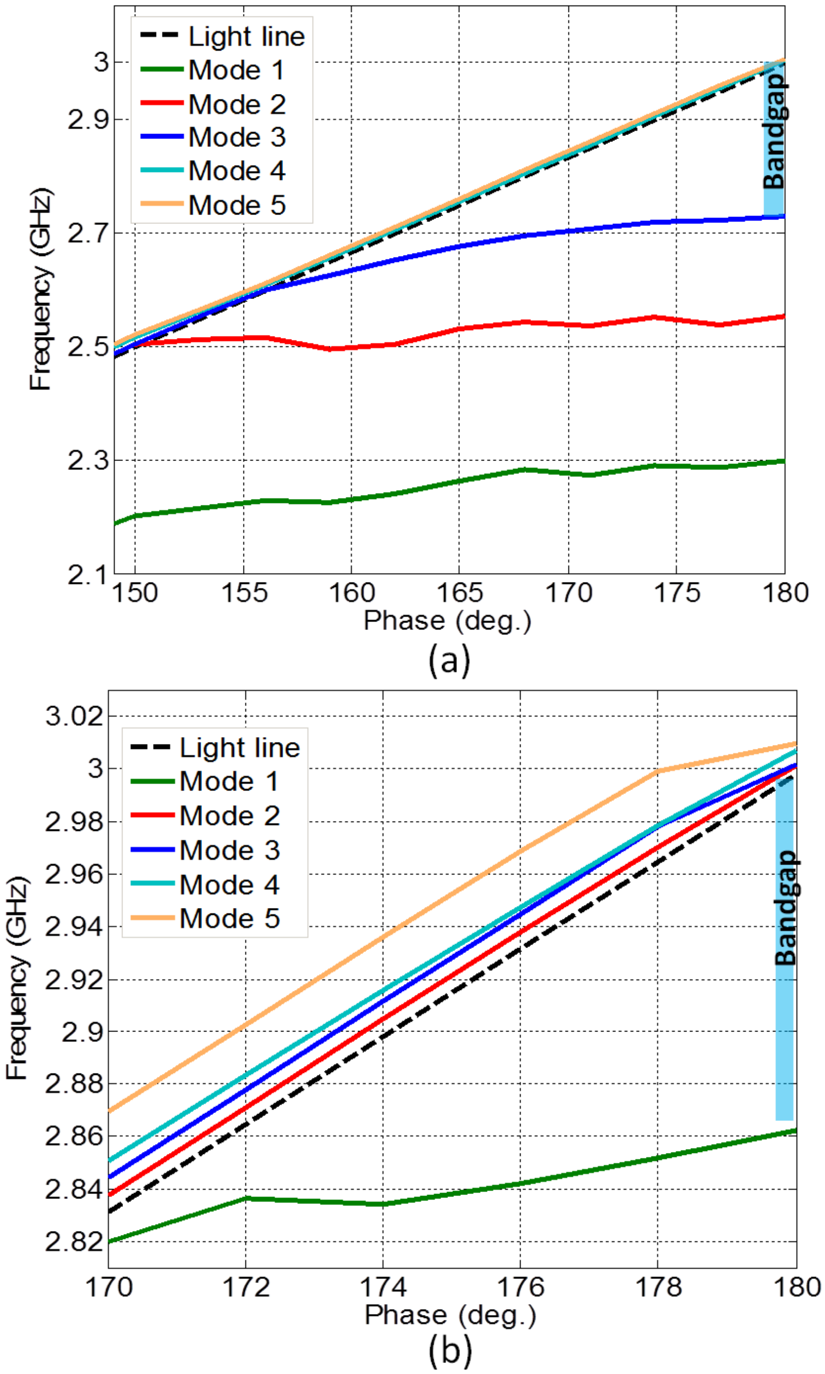

Figure 2.2 Dispersion, along the Γ-X direction, diagram of (a) the uniform substrate and (b) the composite bandgap-antenna structure elements.

Therefore, a complete bandgap cannot be detected, using the HFSS eigenmode solver, from the dispersion diagram directly.

We study the impact of these modes on the bandgap further by using their field profiles as shown in Figure 2.3. An alternative technique, the transmission method, will also be utilized for proper bandgap investigation. Modes 4 and 5 of the uniform substrate seem, from Figure 2.3a, not to be of the unit element structure which is placed at the bottom of the simulation setup, since their fields are maximum in the air region while they are almost zero on the structure. Instead, they may be unphysical or modes of the complete setup rather than that of the unit element structure; in either case, they can be ignored since the main focus is the modes of the unit cell structure. Here mode 3 of the uniform substrate is the one we should take into account;

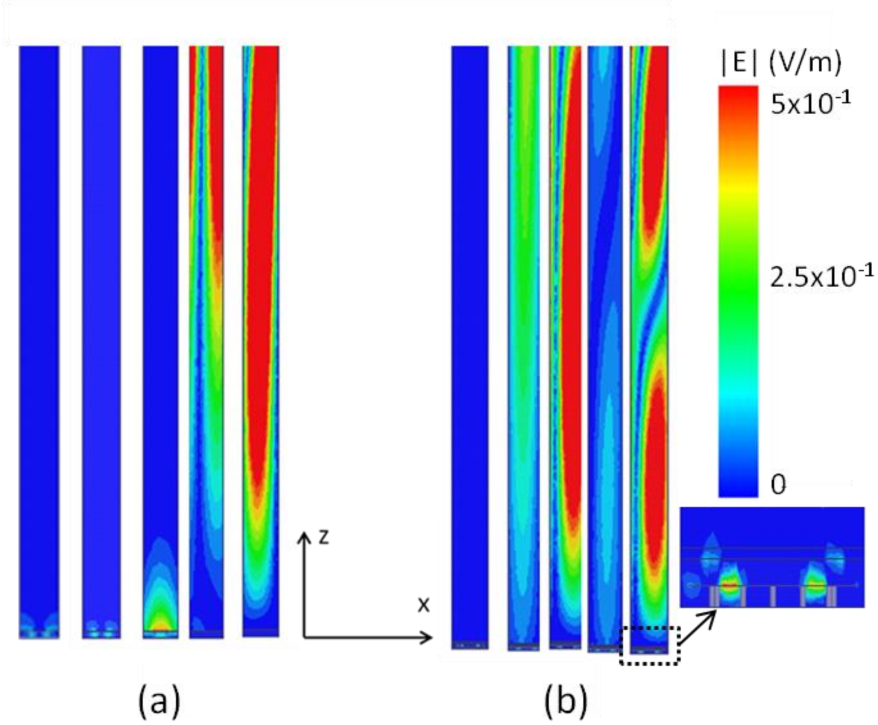

Figure 2.3 Side view of the simulation setup with field patterns of modes 1-5 from left to right at phase of 175° on Figure 2.2 (a) uniform substrate and (b) composite bandgap-antenna structure unit elements. All views, except mode 2 of uniform substrate which is zy-plane view, show zx-plane.

it is the only bound mode that will be effective in the operating frequency band. On the other hand, the first two modes are not effective in the bandgap of interest even though they seem be physical and

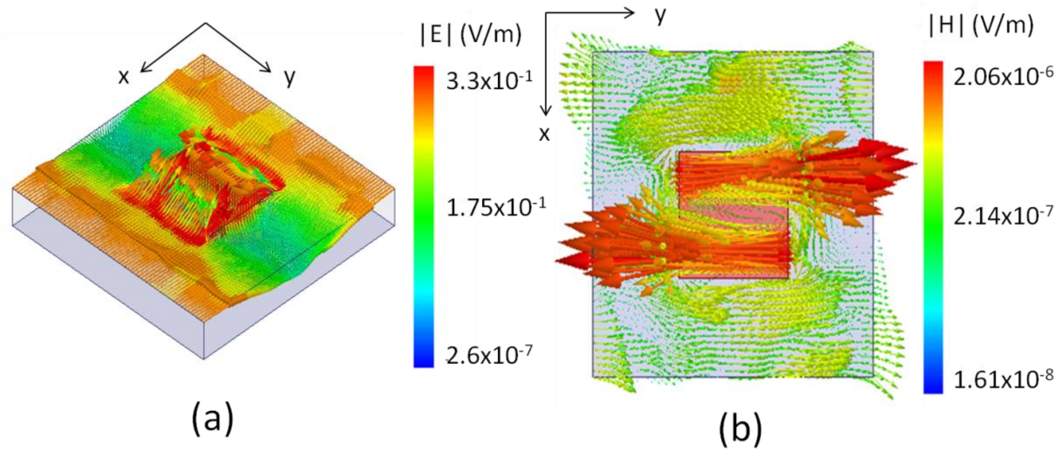

Figure 2.4 Mode 3 of the uniform substrate element. (a) Vector electric field and (b) vector magnetic field distribution.

part of the structure. As a side note, if we analyze this unit cell based on a conventional approach, i.e. a grounded dielectric slab without the top patch, we would obtain only one mode, which corresponds to mode 3 shown in Figure 2.2a, in the bound mode region; but not the first two modes. This mode will be referred in the context of scan blindness in the next chapters; its vector field distribution, shown in Figure 2.4, will provide physical insight into scan blindness. Its electric field vector forms a loop normal to the surface, while the magnetic field vector is parallel to the surface; thus, it is a TM mode, and it induces E-plane scan blindness in microstrip patch phased arrays. Even though it seems that this mode is not propagating in the prescribed frequency band of interest (2.90-3.00 GHz) as shown in Figure 2.2a, it will appear in the band in the X-M section of the dispersion diagram.

We similarly analyzed modes of the composite structure bandgap-antenna unit element as shown in Figure 2.2b. Here only mode 1 is bound and the other 4 modes should be investigated using their field patterns also in order to determine their impact on the bandgap. As shown in Figure 2.3b, mode 1 is bound to the structure while modes 2, 3, and 5 seem to be not that of the unit cell. Mode 4, on the other hand, may be propagating within the unit cell; however, it seems that this mode is more radiative and may not perturb the bandgap. We will use another approach of two-port transmission in order to investigate the impact of mode 4 and any other potential propagating modes further on the bandgap.

2.3 Transmission Analysis of Bandgap-Antenna and Uniform-Substrate Antenna Elements

The transmission setup is illustrated in Figure 2.5, where seven unit elements are placed between two waveports. The setup is terminated using an absorbing material (PML) from the top and radiation boundaries from the back of two waveports; these absorbing and radiation boundaries are employed to capture radiation from the potential leaky waves supported by the structure. Finally, perfect magnetic conductor (PMC) boundaries are used on the sides. The setup shown here can analyze the Γ-X section, which is the most problematic one in our case, as we discussed in the previous section, of the dispersion diagram further. Specifically, to make sure that leaky wave region modes, following the light line and merging at X point on the dispersion diagram, do not cancel the bandgap. Another important feature of the transmission setup is that integrated structures with element size of larger than $0.5\lambda_0$ can be studied, whereas dispersion setup has element size limited to $0.5\lambda_0$ or smaller. On the other hand, the transmission setup can investigate the structures along only the main axes and the diagonal axis, while the eigenmode dispersion approach can consider all possible directions if the geometry satisfies certain symmetries.

The transmission from the uniform substrate patch and composite structure elements is shown in Figure 2.6. The results are normalized to their values at 3.08 GHz, for both uniform and composite structures separately. Considering the frequency band of interest from 2.90 to 3.00 GHz, it is shown that while the uniform substrate elements have almost 0 dB (-1.7 dB at 2.92 GHz) transmission, the composite structure demonstrates the bandgap behavior from 2.95 to 3.02 GHz, where transmission is more than 10 dB lower than that of the uniform substrate. Compared to the conventional bandgap materials, where bandgap is characterized using transmission below -15 or -20 dB with respect to the free space medium, the performance of the composite structure presented here is characterized with -10 dB transmission with respect to the uniform substrate elements, but not the free space medium, as shown in Figure 2.6.

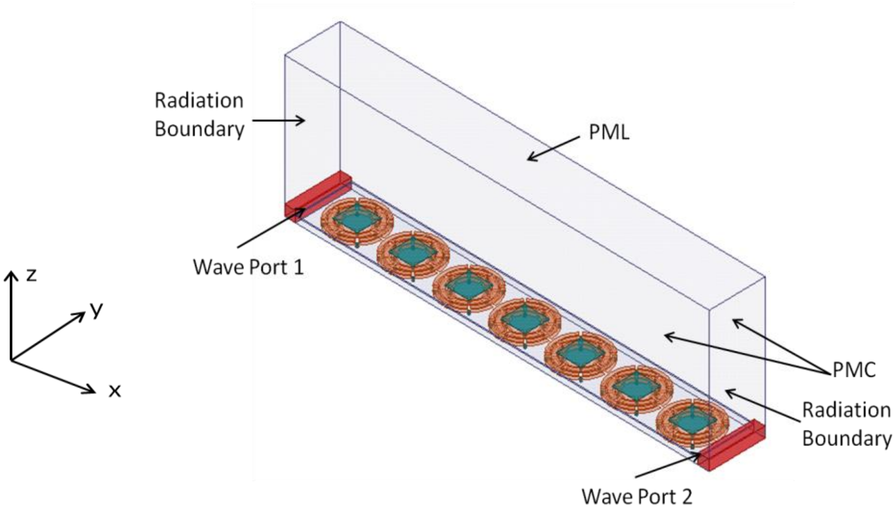

Figure 2.5 Two port transmission setup.

A Comparison of the dispersion results of the Γ-X section, shown in Figure 2.2, with the transmission results of Figure 2.6 can be misleading. Even though the Γ-X and transmission setup analyze the same physical axis (x-axis) along the unit cell array, one should not expect identical bandgap properties from both. The Γ-X section deals with modes propagating along the corresponding axis only; however, transmission setup takes into account modes propagating along this axis and also considers the wave vector components of the waves propagating along the other directions, which

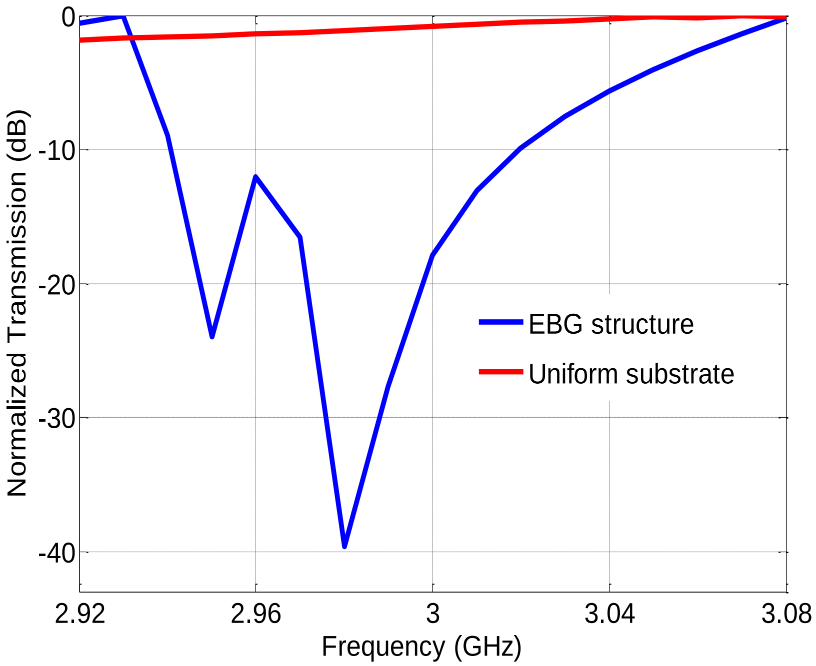

Figure 2.6 Transmission from 7 unit elements for uniform and bandgap-antenna structures.

may not appear on the Γ-X section. For example, transmission from the uniform substrate shows no bandgap (unnormalized results also do not show bandgap); but, the Γ-X section of the same structure, considering mode by field patterns as well, has actually no propagating mode at the frequency region analyzed by the transmission setup. The reason beyond this is that mode 3 of the uniform substrate will appear, as shown in Figure 2.7, in the frequency band within the X-M section of the dispersion diagram; and the transmission setup considers wave vector component of this mode along the axis of propagation as well.

2.4 Omnidirectional Bandgap

Impact of the substrate modes on the bandgap has been analyzed using both eigenmode dispersion and two port transmission methods. However, we have focused on only one direction of propagation so far; but, since the unit elements studied here will be used in planar phased arrays, the bandgap investigation along all directions is needed. For these analyses, we will focus on mode 3 of the uniform substrate element and mode 1 of the composite structure only since the role of the other modes has been cleared, they are not effective, in the previous section. The first two modes of the uniform substrate do not propagate in the frequency band of interest, 2.90-3.00 GHz, therefore they are omitted. All the other modes for both structures remain in the leaky wave region and their behavior has been shown through the field patterns and transmission setup, where they were found to be not effective in the bandgap region of interest.

Figure 2.7 shows omnidirectional dispersion diagram, using reduced triangle Brillouin zone, of the unit cells of the uniform substrate and composite structure elements for mode 3 and mode 1, respectively; the Γ-X, which is along the x-axis, and M-Γ sections are shown partially for the leaky wave regions, since these modes are not stable and the dispersion technique is not fully capable to show modes in the leaky wave region properly.

Uniform substrate, with the top patch on, has a propagating mode in the X-M region of the diagram, which corresponds to the propagation directions for angles between 0° to 45° from the x-axis, and this mode is propagating for the entire frequency band of interest. It shows similar characteristics as for the fundamental TM_0 mode of the grounded dielectric substrate, considering its field profile in Figure 2.4. This propagating mode shown here is identical along the x- and y- directions since the top patch and substrate sizes are square. In the context of a microstrip phased array, however, it is more effective along one direction (x- or y-), depending on the feeding position. If, for example, the structure will be excited along the x-axis, excited radiating currents on the patch surface will be along the x-axis for the dominant Floquet modes and they will couple to and excite this substrate mode, shown in Figure 2.7, along the x-axis only, the substrate mode along the y-direction will remain unexcited. Therefore, the coupling through the substrate modes is more effective along the E-scan plane. This point will be explored more and linked to the scan blindness phenomena in the next chapters.

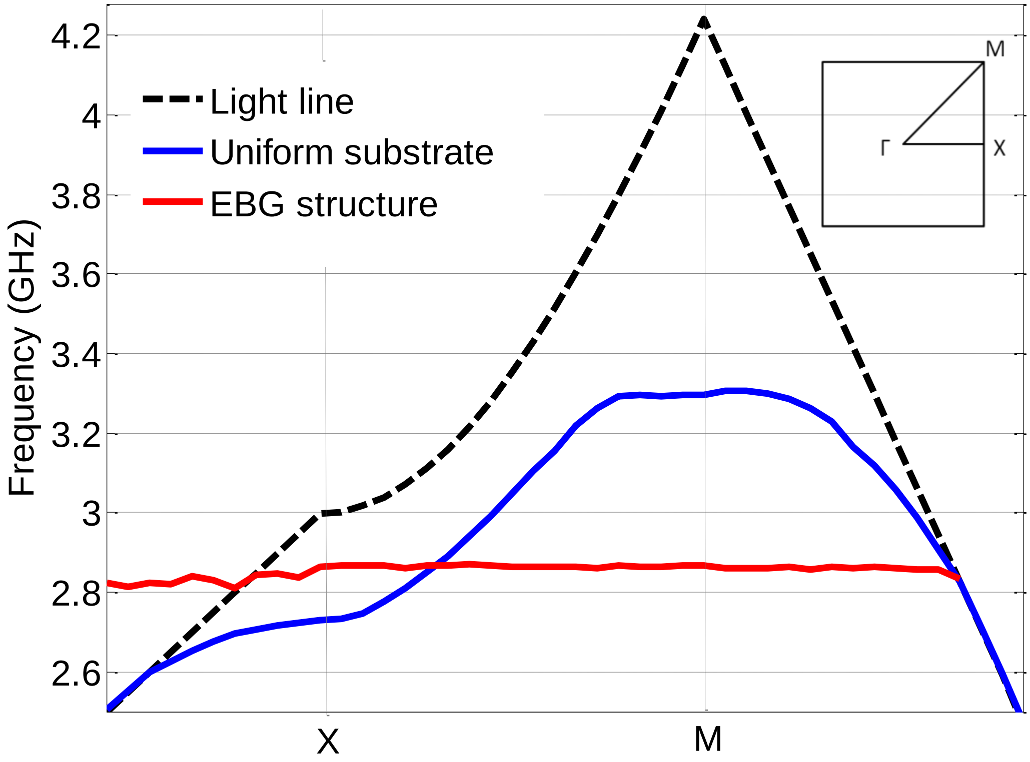

Figure 2.7 Omnidirectional dispersion diagram of the bandgap-antenna and uniform substrate elements.

In order to eliminate this mode, propagating within the uniform substrate at the operating frequency band, we use the composite structure of Figure 2.1, which is investigated with its all parts, including vias and top patch. The grounding vias are essential and bandgap disappears if they were not used. Similarly, the top patch should also be used to obtain the complete bandgap.

As shown in Figure 2.7, the composite bandgap-antenna structure completely eliminates the mode along all directions from 2.87 to 3.00 GHz with the stop bandwidth of 4.4%.

Even though dispersion diagram shown in Figure 2.7 demonstrates the bandgap from 2.87 to 3.00 GHz for the composite structure, it is narrower, 2.95-3.02 GHz, in the transmission setup shown in Figure 2.6. This may be due to leaky waves supported by the structure which are effective in the transmission setup while they are not considered in Figure 2.7; however, these leaky waves are not strong as shown through their field patterns in Figure 2.3. The reason of the narrower bandgap width of the transmission could also be due to internal couplings between metallic parts within a unit cell, where these couplings can be along the normal direction, between different metallic layers, such that energy can be stored instead of being propagated; therefore these kinds of internal couplings cannot be detected by dispersion analysis but they are physically effective. Also, note that eigenmode dispersion and two port transmission setups are not identical as explained above, due to effective wave vector components in transmission setup only; however, this should not be the reason beyond the bandgap differences since there is no mode, so does its components, available within the bandgap.

In fact, the transmission setup has another bandgap (below -10 dB transmission) centered at 2.90 GHz. However this bandgap is only from 2.89 to 2.91 GHz and disconnected from the one shown in Figure 2.6. The disconnected spectrum range is from 2.91 to 2.95 GHz. We will utilize the complete, for both bound and radiating modes, and omnidirectional frequency bandgap from 2.95 to 3.02 GHz for elimination of the scan blindness in the next chapters. However, we still believe that the structure has actually a practical omnidirectional bandgap, for propagation along the *lateral* directions, from 2.87 to 3.02 GHz.

We will use the bandgap-antenna structure as a radiating element for a phased array where there will be no coupling between the elements through the propagating substrate modes, therefore it provides scan blindness-free phased arrays. Within omnidirectional bandgap, lateral wave vector is $k_{\|} = 0$; thus, radiation from the structure will be normal to its surface.

2.5 Conclusion

A multifunctional structure which is capable of behaving as a bandgap structure, suppressing both bound and radiating wave modes along the lateral directions, and an antenna element, radiating to the broadside direction, for scan blindness-free phased arrays has been presented. Unit cell of the structure has been analyzed in detail; its geometrical and material features has been explained. Modal characteristics of the structure were analyzed through eigenmode, field profiles, and two port transmission techniques. Combining the results of these methods, we found that the proposed bandgap-antenna structure has a complete bandgap along all directions for substrate waves propagating laterally. This structure will be used as an antenna element in a phased array environment for scan blindness elimination in the next chapters.

Chapter 3

Radiation Characterization of Bandgap-Antenna Element

This chapter focuses on the radiation characterization of the proposed multifunctional, or the bandgap-antenna, structure. As mentioned in the previous chapter the structure does not propagate any mode along the lateral directions; however, it supports radiation normal to its surface. In fact, its radiation properties are similar to that of a conventional microstrip patch antenna. The center of the structure does not contain any radiating or bandgap metallization, where a coaxial probe is used to feed the structure as shown in Figure 3.1. All configurations and sizes remain same as the structure used for modal and bandgap investigation in the previous chapter. As such, lateral sizes, in a square shape, are half-wavelength at 3 GHz (50 mm), which is required for the dispersion and scanning analyses. The only modification in this chapter is the

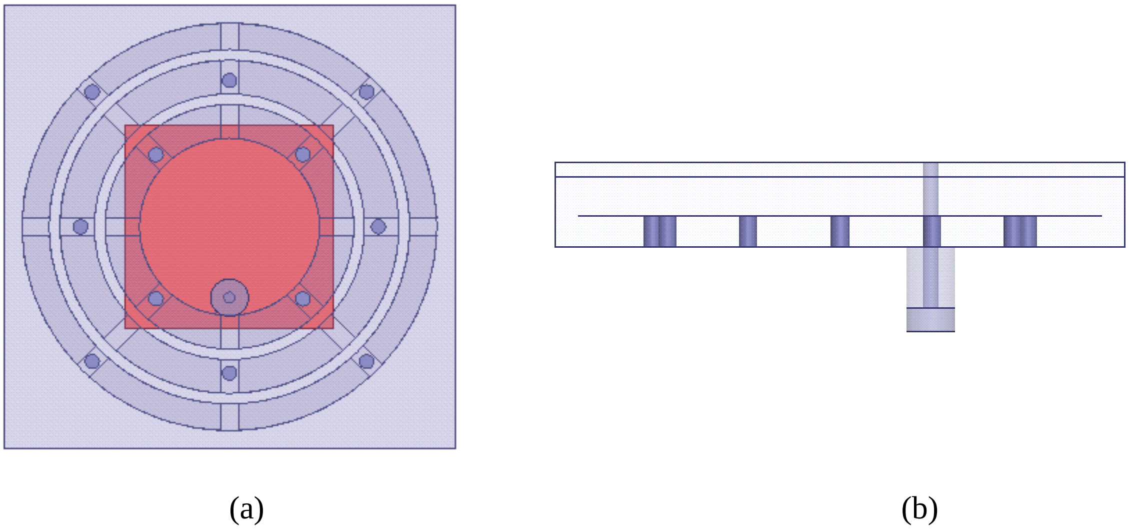
(a) (b)

Figure 3.1 Bandgap-antenna structure with a coaxial feeding probe. (a) Top and (b) side views.

feeding probe within the substrate. We further used an impedance matching network in order to match the structure input impedance to 50 Ω; this matching network layer is an additional layer so that it does not affect bandgap-antenna element's modal and bandgap characteristics. Additionally, the feeding probe also does not affect structure's modal and bandgap properties as discussed in the previous chapter.

The single element operating frequency is chosen to be 2.99 GHz, which is within the bandgap frequency range of 2.95-3.02 GHz, and it is below half-wavelength frequency (3 GHz) of the structure whose size is 50 mm along the x- and y- directions. This working frequency should be very close to half-wavelength at 3 GHz for scanning investigations in the next chapter. Since we will focus on scan blindness, if the substrate size or inter-element spacing is reduced too much, or the operating frequency is chosen much lower than 3 GHz, scan blindness disappears and performance of the structure cannot be evaluated. Overall, the single element radiation performance is analyzed at the center frequency of 2.99 GHz throughout this chapter.

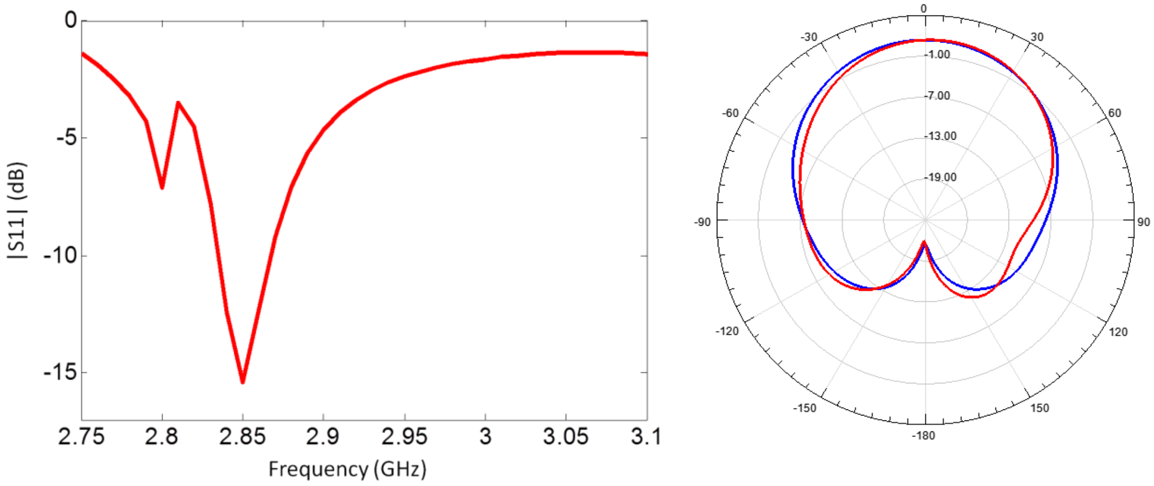

(a) (b)

Figure 3.2 (a) Input reflection coefficient and (b) realized gain (dBi) of the bandgap-antenna structure shown in Figure 3.1.

3.1 Impedance Matching Network Design

The reflection coefficient and radiation pattern of the proposed bandgap-antenna structure, that is shown in Figure 3.1, are shown in Figures 3.2a and 3.2b, respectively. From the reflection coefficient, we can see that it resonates as a radiating element at 2.85 GHz, far away from the desired working frequency of 2.99 GHz. However, its radiation pattern at 2.99 GHz, shown in Figure 3.2b, is still like that of a conventional patch antenna. The realized gain at the desired frequency is 1.37 dBi and its reflection coefficient is only -1.72 dB at the same frequency. Therefore, it requires a matching network in order to operate efficiently at 2.99 GHz. It is worth noting that the notch observed from the reflection coefficient at 2.80 GHz is due to the concentric rings in the substrate for the bandgap purposes. In fact, this notch was shifted from the frequency band of interest near 3 GHz to around 2.80 GHz by introducing cuts into the concentric rings of both layers.

A stripline network is used for impedance matching as shown in Figure 3.3, where it is fed by a waveport from the edge. Rogers TMM3 ($\varepsilon_r = 3.27$, $\tan\delta = 0.002$) with total thickness

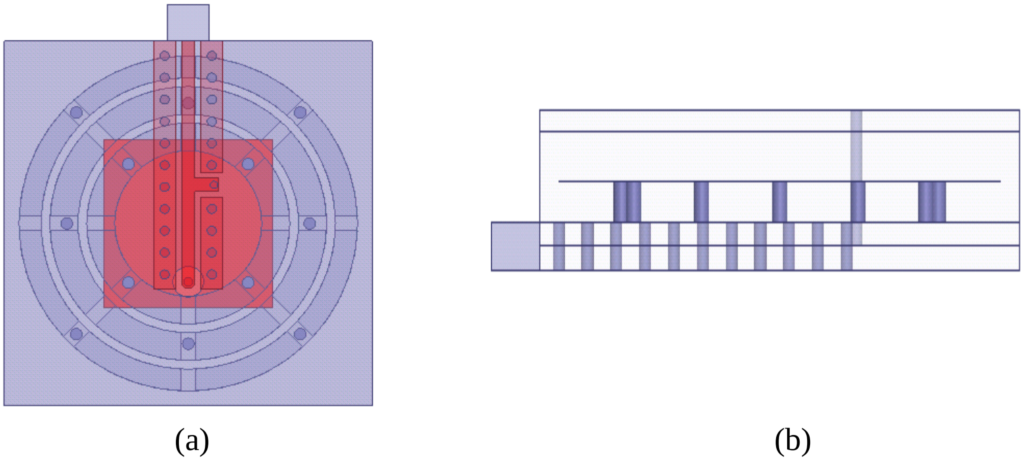
(a)

(b)

Figure 3.3 Bandgap-antenna structure with edge-fed stripline impedance matching network. (a) top view, (b) side view.

of 3.048 mm is used as a dielectric substrate for the stripline design where the stripline trace is placed in the middle of the dielectric. The stripline has 50 Ω characteristic impedance and thus its width is 1.8 mm. Before introducing a matching network stub into the stripline layer, we measured the input impedance of the structure near the probe, feeding the radiating top patch, by de-embedding the measurement plane 32 mm from the waveport. The simulated de-embedded input impedance is 226+j246 Ω at 3.00 GHz. To design the matching network, this impedance is then used as a load impedance in a network simulator (Microwave Office AWR) in order to determine the shorted stub length and its position from the load, which are 3.2 mm and 11.4 mm,

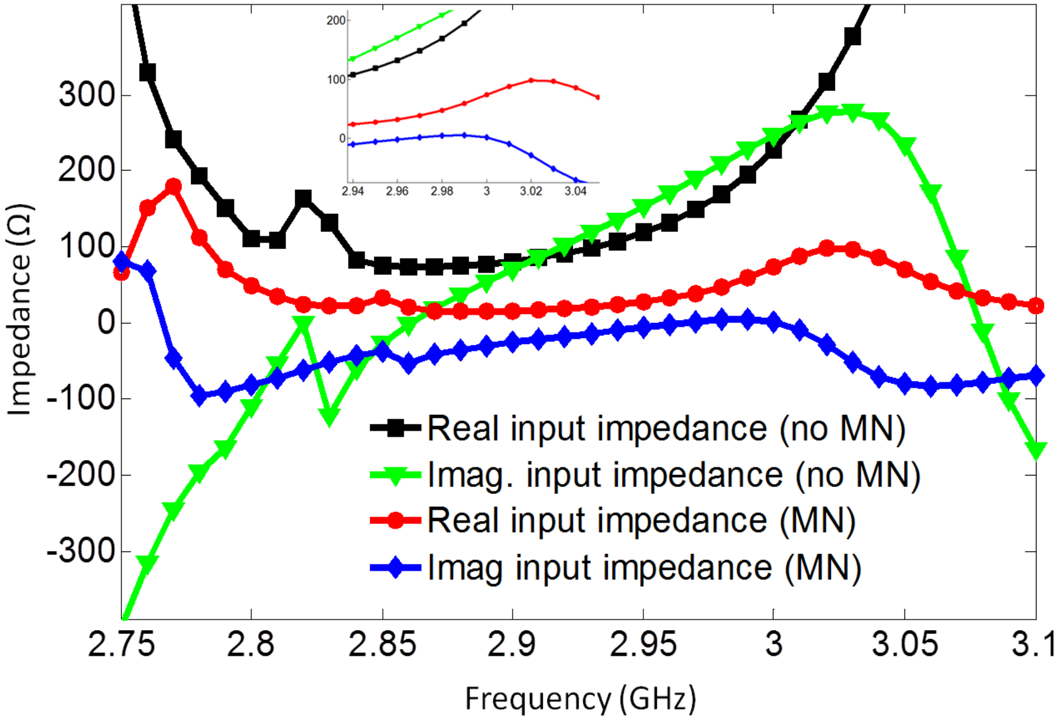

Figure 3.4 Input impedance, measured at the waveport plane, of the radiating-bandgap structure with and without impedance matching stub in the stripline network.

respectively. The structure with matching network, depicted in Figure 3.3, has input impedance of 59+j5 Ω at the waveport plane. Figure 3.4 further illustrates the performance of the matching network where the input impedance, measured at the waveport plane, is shown for the stripline without and with the shorted stub; where the inset shows that impedance matching to 50 Ω for the frequency region of interest centered at 2.99 GHz is successful. Figure 3.5 shows the effect of the matching network on the gain of the structure; for the edge-fed stripline without the matching stub, gain at broadside is 1.47 dBi while it increases to 6.08 dBi for the edge-fed stripline with impedance matching stub; and to 6.12 dBi in the case of coax-fed stripline with impedance matching stub as will be explained in Figure 3.6.

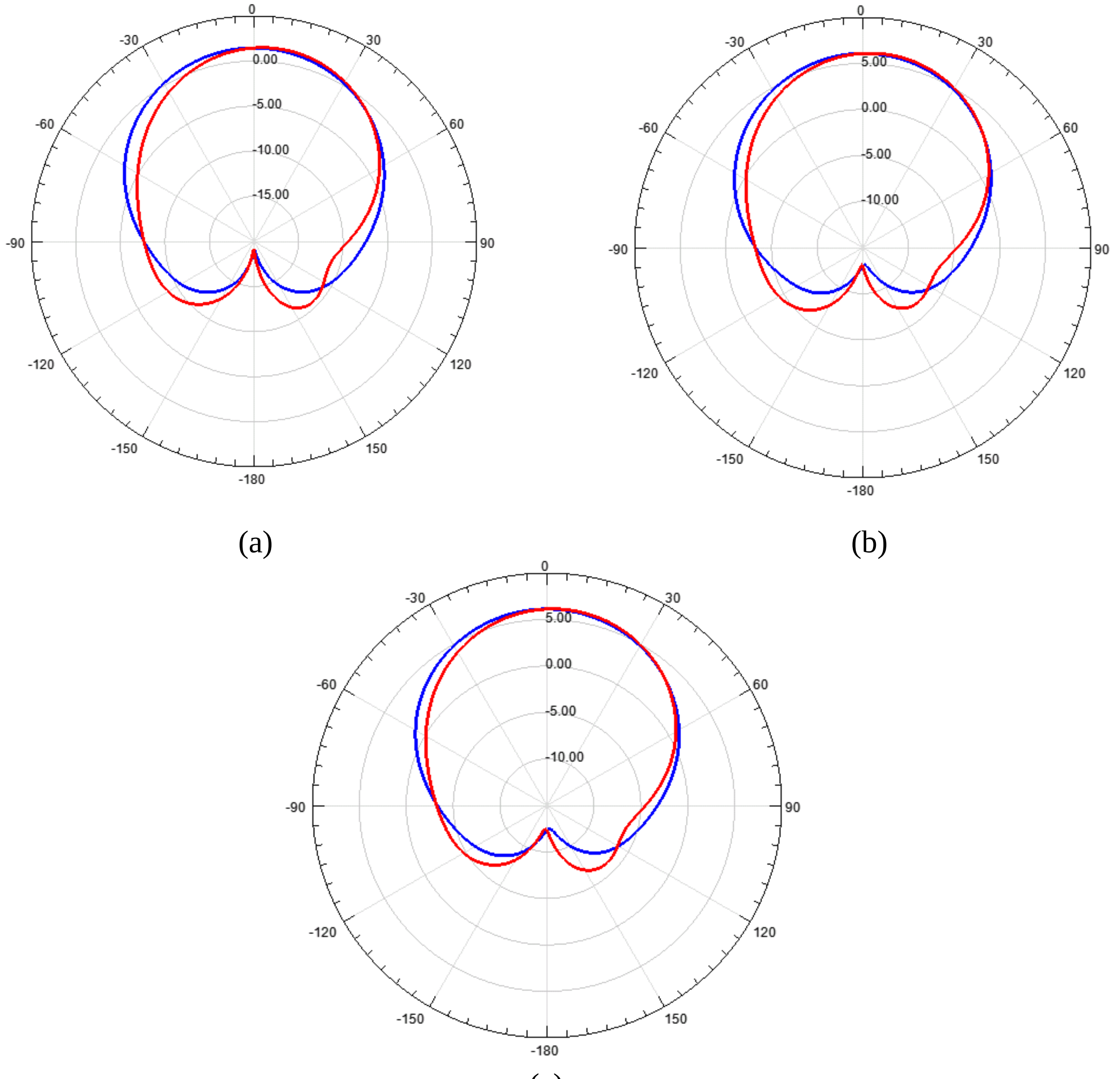

(a)

(b)

(c)

Figure 3.5 Realized gain (dBi) pattern of the stripline fed bandgap-antenna structure. (a) Edge-fed no stub, (b) edge-fed with stub, and (c) coax-fed with stub.

3.2 Coax to Stripline Transition Design

The edge-fed stripline was necessary to obtain element input impedance to design the matching network; however, we will feed the structure using a coaxial probe, which is more practical for experimental demonstration, from the bottom. More importantly, this unit element

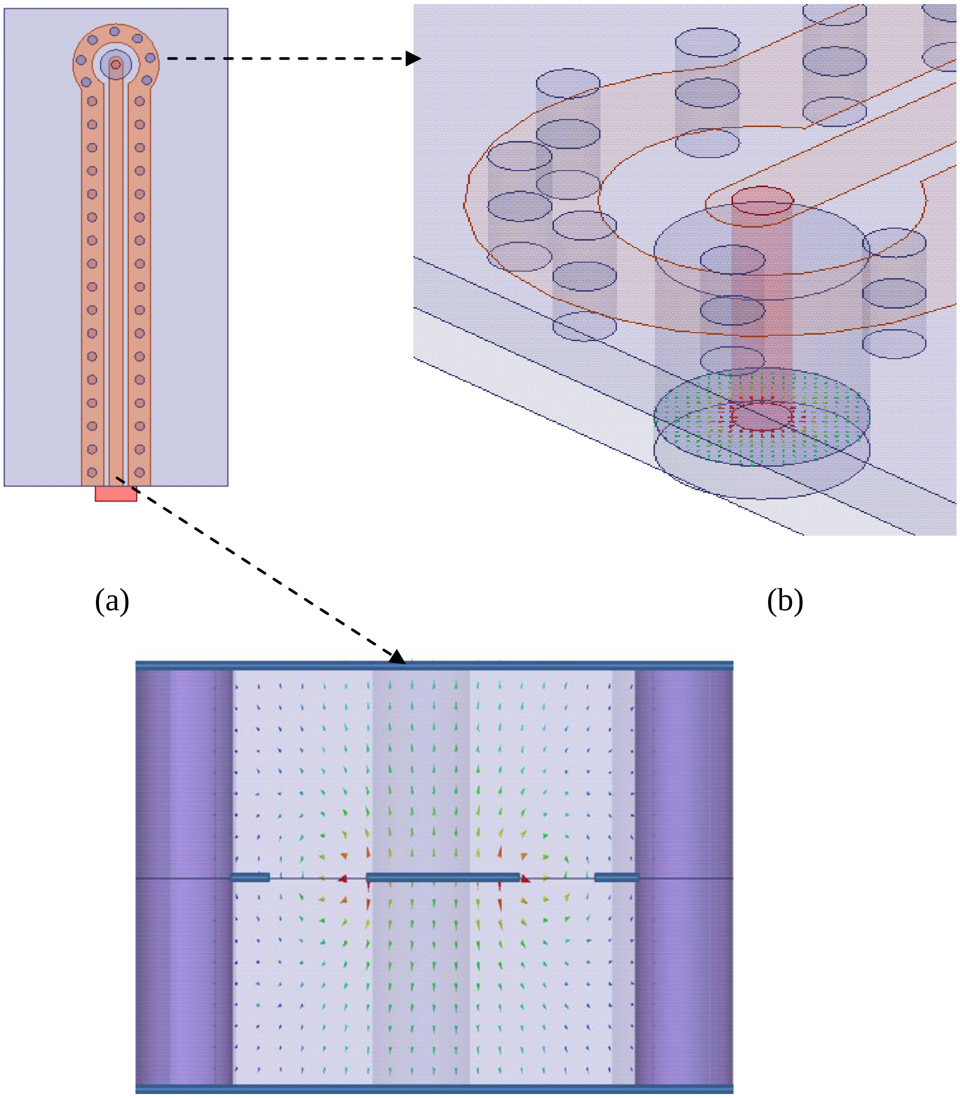
(a)

(b)

(c)

Figure 3.6 Coax to stripline transition. (a) top view, (b) perspective view of the coaxial feed, and (c) stripline excitation port. Vector electric fields of the excited modes of the coaxial and stripline are shown.

will be used in planar array configurations where the array system needs other modules, such as beam forming network. Therefore, it is essential to shield all these feeding mechanisms from the radiating layer. We still use stripline matching network presented in Figure 3.3; however, now it will be excited using a coaxial probe. In order to achieve this, a stripline to coaxial transition, shown in Figure 3.6, is used. We note that all the material and geometrical parameters of the stripline remain same as the one shown in Figure 3.3. Figures 3.6b and 3.6c further illustrate modal field profiles of coaxial and stripline feeds. The performance of the transition is shown in Figure 3.7, where transmission and reflection are better than -0.18dB and -20dB from 1 to 7 GHz, respectively. Specifically, they are -0.07 dB and -26.35 dB at the operating frequency of 2.99 GHz, respectively. This coax to stripline transition will be incorporated with the impedance matching network in order to obtain practical feeding mechanism for the proposed composite structure.

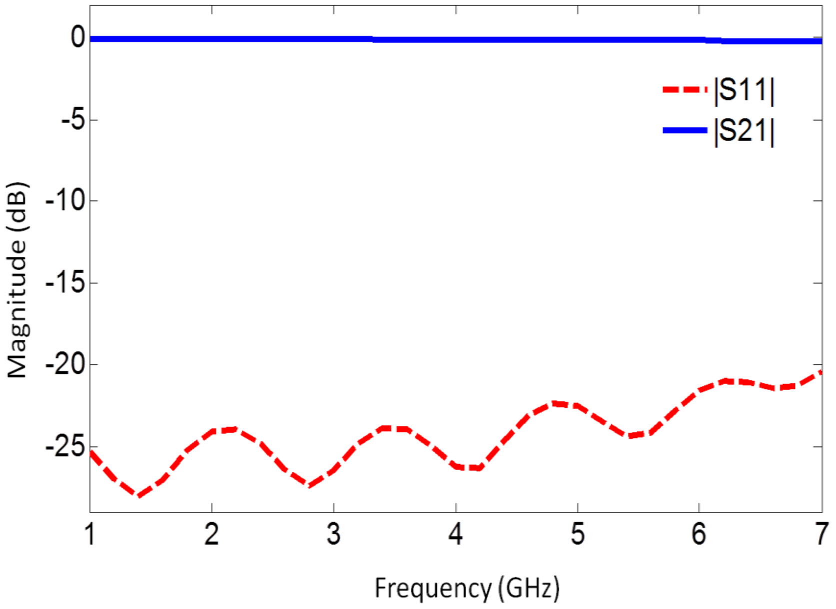

Figure 3.7 Transmission and reflection coefficients of the coax to stripline transition.

3.3 Bandgap-Antenna Element with Impedance Matching Network

Ultimate radiating element with the matching network is shown in Figure 3.8. The matching network, stub length and its position from the feeding probe, is the same as the one fed from the edge and shown in Figure 3.3. Since the transition is well behaved, we expect that the element performance for the edge-fed and coax-fed cases to be similar. Indeed, that is the case as illustrated in Figure 3.5, where radiation patterns are similar for both cases and the peak realized gain values are very close to each other, 6.08 dBi for the edge-fed and 6.12 dBi for the coax-fed cases. The structure of Figure 3.8 will be used for the array investigations and experimental demonstrations. Therefore, it is essential to elaborate its radiation mechanism further. In fact, we already saw that the proposed structure has similar radiation pattern as a conventional patch antenna, radiating to broadside.

Figure 3.9 shows that a conventional patch antenna on a uniform substrate and the structure of Figure 3.8 have similar electric field (magnitude) distribution on the surface of their substrates. This justifies that the proposed structure can be considered as a patch antenna but

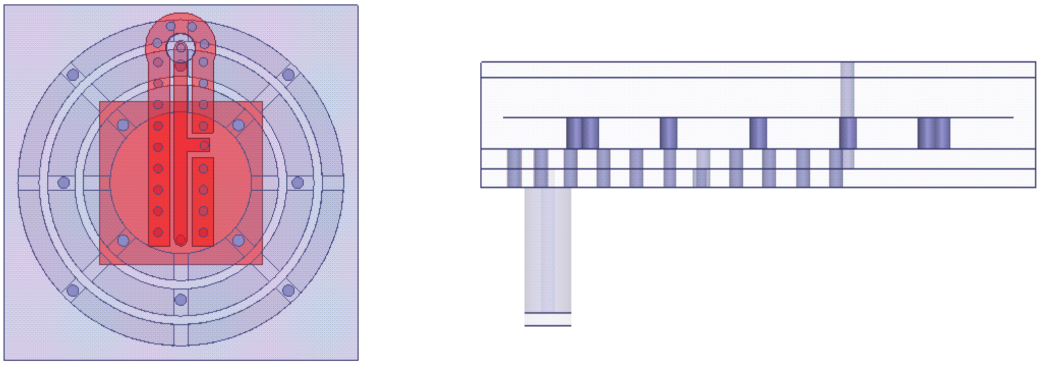
(a) (b)

Figure 3.8 Radiating-bandgap structure with a coax fed, through a coax to stripline transition, and the stripline matching network. (a) Top and (b) side views.

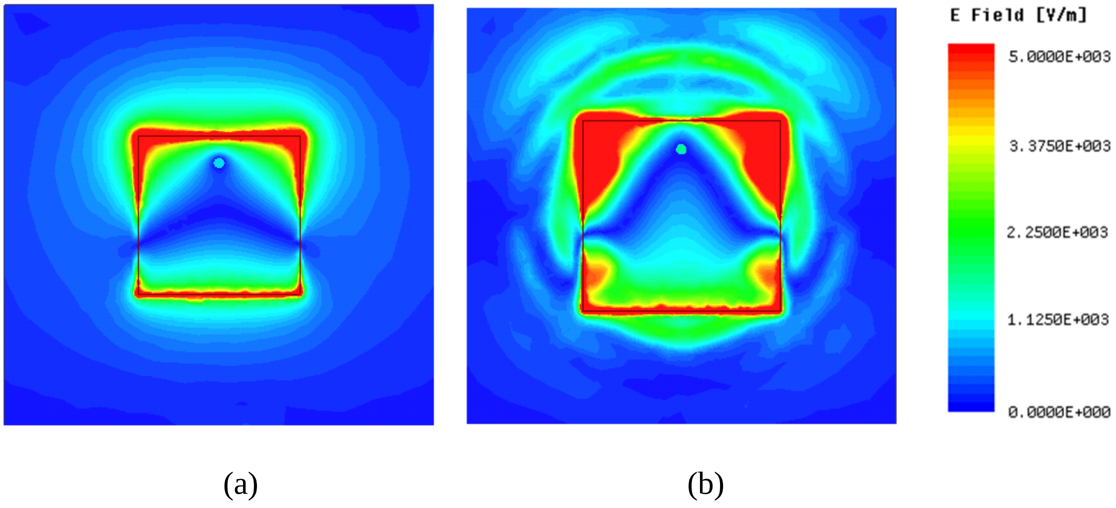

Figure 3.9 Electric field (magnitude) distribution on the surface of (a) uniform substrate patch antenna and (b) coax-fed radiating-bandgap structure, of Figure 3.8, with impedance matching network.

different from the conventional patch antenna by not supporting propagating substrate modes. Since the substrate modes result in losses and pattern degradations, one should expect that the proposed structure is actually behave better, in terms of improved gain and smoother radiation patterns.

Figure 3.9b further explains that there is coupling between top patch and embedded rings where there are localized ring shaped electric field patterns. These coupled fields, to the rings, should not be considered as propagating substrate modes. In fact, they radiate to the space from the ring surfaces instead of being propagated in the substrate. Moreover, these couplings to the embedded rings reduce the radiation efficiency. On the other hand, the electric field distribution of the conventional patch antenna in Figure 3.9a implies that the substrate modes, or shown electric field pattern, are not that localized and effective in the substrate.

In order to complete the radiation characterization of the bandgap-radiating structure, we compare its radiation properties with that of a conventional patch antenna in Figures. 11, 12, and

13. Effect of thte matching network can also be viewed from these figures; another important observation is elements with edge and coax feeds have similar behaviors.

As mentioned before, operating frequency of the element is chosen to be 2.99 GHz; the reason beyond that is the coax-fed element with the matching network, which is the ultimate

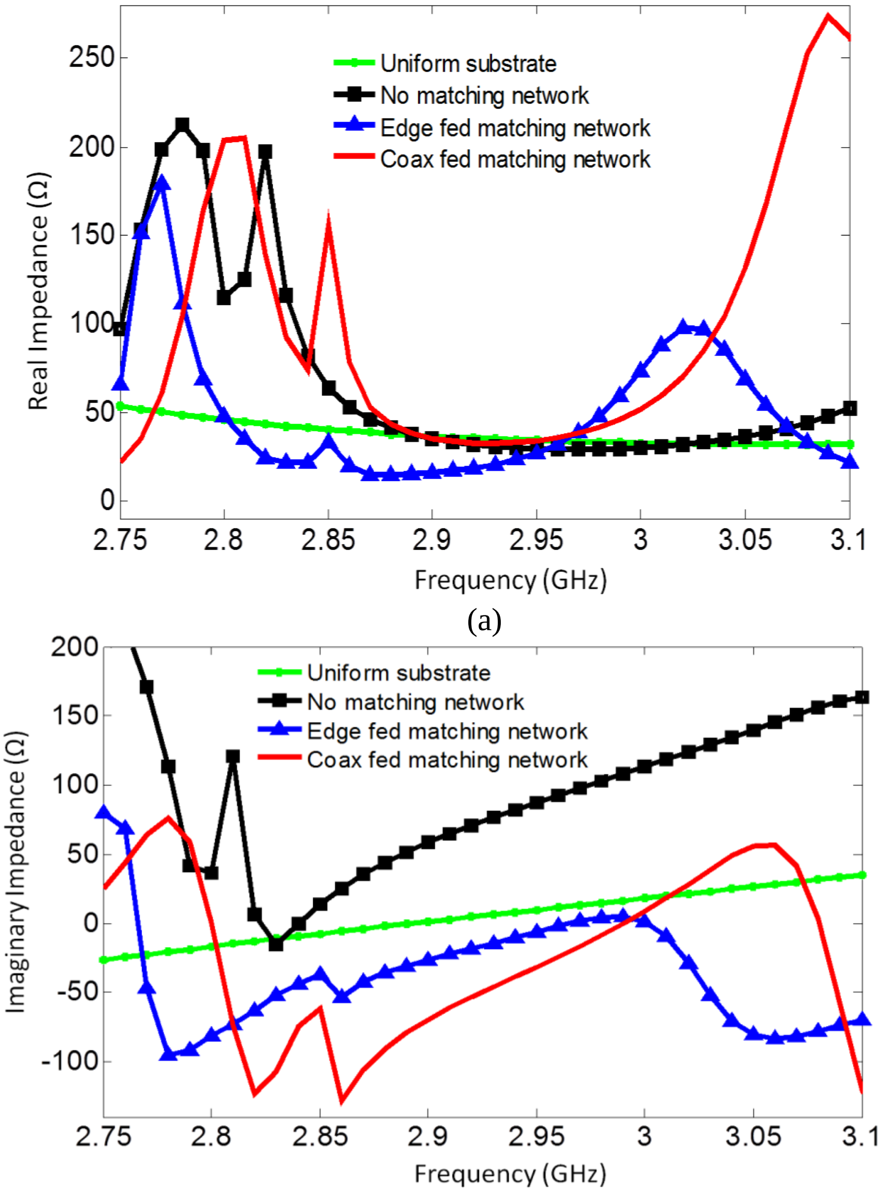

(a)

(b)

Figure 3.10 Radiating element input impedances, (a) real and (b) imaginary, for different structures: Uniform substrate conventional patch antenna, no matching network (structure of Figure 3.1), edge fed matching network (structure of Figure 3.3), and coax fed matching network (structure of Figure 3.8).

design, resonates at this frequency as shown in Figure 3.11 while the one fed from the edge resonates at 2.98 GHz. On the other hand, resonance frequency of the conventional patch antenna element is 2.86 GHz. Both this conventional patch antenna element and the coax fed element with matching network will resonate at the same frequency of 2.96 GHz in an infinite array environment. The frequency shift between element and array cases is more significant in the uniform substrate conventional patch antenna; this is due to induced couplings through the substrate modes, i.e. leaky or surface waves, in the case of uniform element array configuration. This point will be elaborated more in the next chapter.

As can be seen from these figures, composite structure, of Figure 3.1, without any matching network is more efficient at frequency of 2.85 GHz where it actually provides more peak gain than conventional patch antenna. We note that we do not have more flexibility to modify this structure for impedance matching, since it has already been co-designed with

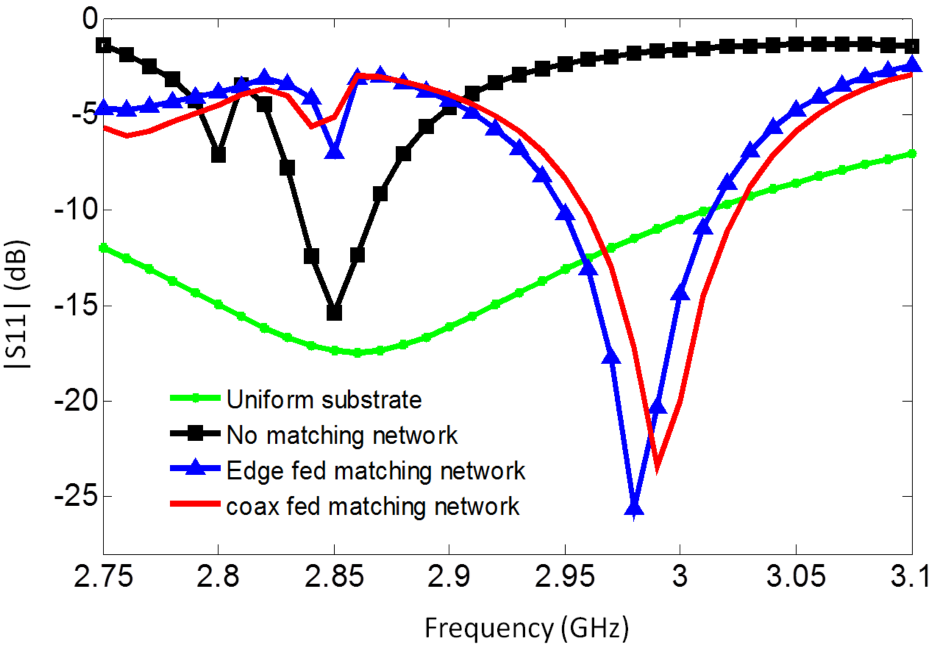

Figure 3.11 Reflection coefficient for different structures: Uniform substrate conventional patch antenna, no matching network (structure of Figure 3.1), edge fed matching network (structure of Figure 3.3), and coax fed matching network (structure of Figure 3.8).

consideration of the bandgap properties. Therefore, we used the stripline matching network which is well isolated from the bandgap-antenna structure and does not affect its bandgap properties but enhances its radiation properties. Since the matching network is designed for the input impedance measured at 3 GHz, edge and coax fed structures with matching network have close impedance, reflection coefficient, and realized gain values at this frequency. In fact, even though impedances deviate from each other slightly, reflection coefficients and realized gains remain close to each other for the entire frequency band shown.

In all cases, the composite bandgap structures provide larger peak gains than conventional patch antenna; this is mainly attributed to the eliminated substrate modes from the composite structures while they carry power and reduce the gain in conventional patch antennas.

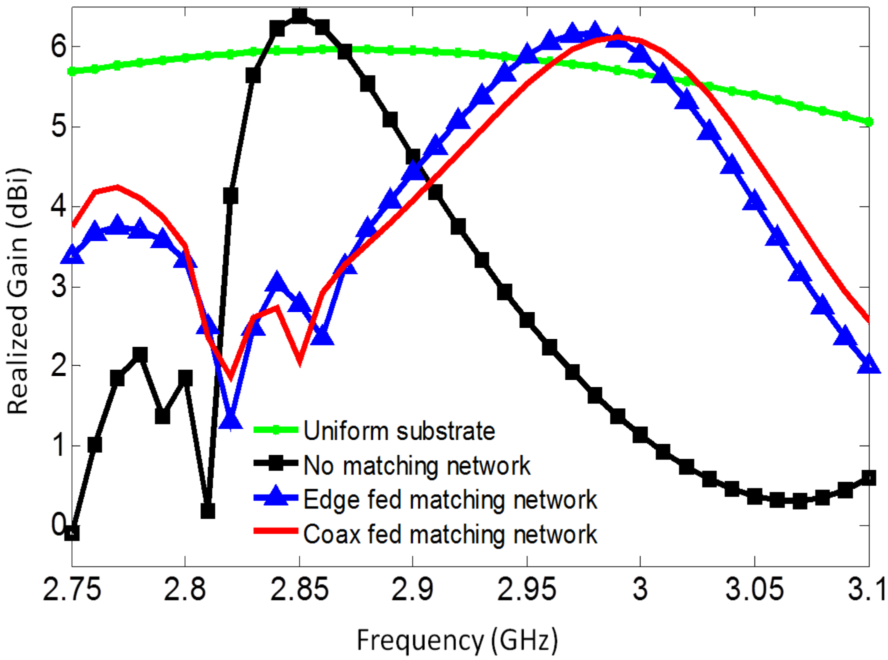

Figure 3.12 Realized gain versus frequency for different structures: Uniform substrate conventional patch antenna, no matching network (structure of Figure 3.1), edge fed matching network (structure of Figure 3.3), and coax fed matching network (structure of Figure 3.8).

Radiation characteristics of all these four different structures discussed here are summarized in Table 3.1 at the element operating frequency of 2.99 GHz. The structure of interest is the one fed with coax and has the impedance matching network, shown in Figure 3.8. Its characteristics at 2.99 GHz are as follows. It resonates at 2.99 GHz where |S11| = -27 dB, -10 dB impedance band is from 2.96 to 3.02 GHz, its realized gain and radiation efficiency are 6.12 dBi and 93.39%, respectively. This element will be used in an array configuration in the next chapter to improve array behaviors.

It is important to note that surface waves are more effective near the scan blindness angles as will be discussed in the next chapter. At broadside, for example, radiation efficiency of the uniform substrate patch antenna can be higher than that of the bandgap-antenna element as illustrated in Table 3.1 for the isolated elements, the performance of the bandgap structure will show up at larger scan angles. The lower radiation efficiency of the composite structures in Table 3.1 is mainly due to couplings, between the different metallic layers, within the unit element structure.

Table 3.1 Radiation characteristics of different structures at 2.99 GHz.

	Uniform Sub.	**Composite Sub. No MN (Coax Fed)**	**Composite Sub. Edge Fed MN**	**Composite Sub. Coax Fed MN**
Impedance (Ohm)	32.83+j16.45	29.48+j108.13	59.24+j5.10	45.85-j0.36
|S11| (dB)	-11.00	-1.72	-20.33	-27.24
Bandwidth (GHz) (|S11|=-10dB)	2.71-3.01	2.834-2.867	2.948-3.015	2.96-3.024
Realized Gain (dB)	5.70	1.37	6.10	6.12
Efficiency (%)	98.37	93.49	92.90	93.39

3.4 Conclusion

Radiation characteristics of the bandgap-antenna structure have been studied in this chapter. Before analyzing the radiation performance, an impedance matching network has been incorporated with the bandgap-radiating structure so that its input impedance is matched to 50 Ω. The matching network is employed in the stripline in order to avoid any couplings within the matching network layer. Radiation analyses showed that the bandgap-antenna structure radiates to broadside, similar to a conventional patch antenna; comparisons with the uniform substrate conventional patch antenna further supported performance enhancement of the proposed composite structure. For example, its peak gain is better than that of the uniform substrate patch antenna and electric fields distribution on its surface are more localized, which implies reduction of the substrate modes from the bandgap-antenna structure. The proposed structure with a coax-fed impedance matching network will be used in a phased array environment in the next chapter for the scan blindness elimination.

Chapter 4

Infinite Array Scan Analysis

Microstrip phased arrays' scan range is limited by the electromagnetic waves propagating within the array structure. Excitation of these waves requires certain feeding mechanisms, however as phased arrays are scanned these undesired substrate modes will be excited and limit the scan range of the array by inducing scan blindness. In this chapter, uniform substrate and the bandgap-antenna element based planar infinite phased arrays are investigated in order to shed light onto the substrate modes and their effects, and show how the proposed bandgap-antenna element can successfully suppress propagation of electromagnetic waves from the array substrates so that solve the scan blindness problem.

4.1 Phased Array Modes and Their Effects

There are two distinct types of modes related to the microstrip phased arrays. Radiation from the arrays can be considered as an infinite number of Floquet modes. Electromagnetic waves propagating in a phased array structure are another types of modes. These two sets of modes and their coupling effects will be discussed next.

4.1.1 Radiation Modes

Radiation modes representing the array periodicity field are also known as Floquet modes. In other words, the total array field can be decomposed into an infinite number of Floquet modes. Indeed, each of these modes behaves as a plane wave with corresponding wavenumber and propagation direction. Practically only the first few of these modes couple to air as radiation; the remaining modes are evanescent so that they decay exponentially in the air medium above the array structure while carrying energy and propagating on the array surface. The scanned main beam in phased arrays is due to fundamental Floquet modes while well known grating beams are of the higher order Floquet modes, which are propagating in the air medium. Regardless of whether Floquet modes are propagating or non-propagating in air medium, their tangential, to the array surface, wave number components vary with excitation phase of the array elements as derived in chapter 1,

$$k_{xpq} = k_0 \sin\theta_0 \cos\varphi_0 + \frac{2\pi p}{d_x} \tag{4.1}$$

,

$$k_{ypq} = k_0 \sin\theta_0 \sin\varphi_0 + \frac{2\pi q}{d_y}, \tag{4.2}$$

$$k_{pq} = \sqrt{\left(k_{xpq}\right)^2 + \left(k_{ypq}\right)^2}, \tag{4.3}$$

where each Floquet mode is specified by (p,q) modal indices; d_x and d_y are element spacing along the x- and y- directions, respectively, and (θ_0, φ_0) is the main beam or $(0,0)$ Floquet mode pointing direction. (4.1) and (4.2) describe that direction of propagation of the excited Floquet modes vary with scan angle, thus with elements excitation phase.

4.1.2 Substrate or Structural Modes

Another distinct type of modes supported by the array structure are guided modes propagating within the array substrate; these modes can be either completely bound to the array structure and not couple to surrounding air medium or can also couple to air by radiation. Namely, these modes are known as surface wave (bound) and leaky wave (radiating) modes. It is important to distinguish that Floquet modes are a decomposition of the array field (which is desired to be radiated) and they are excited through excitation of array elements. Surface wave and leaky wave modes, on the other hand, are not desired in the context of the phased arrays considered in this thesis.

The properties of substrate modes supported by the array structure are determined by the element material and geometry profiles. More specifically, substrate thickness and dielectric constant are the main parameters that affect substrate mode behavior. For example, a grounded dielectric material, which has been used to characterize surface wave modes for the phased arrays considered in literature, supports only the fundamental TM_0 surface wave mode if its thickness satisfies the condition

$$d < \frac{\lambda_0}{4\sqrt{\varepsilon_r - 1}}. \tag{4.4}$$

Thicker substrates with greater dielectric constant support higher order modes and effect of the lower order modes will also be more significant on the radiation and scanning characteristics of the phased arrays.

Even though, grounded dielectric materials used as practical printed patch antenna substrates are thin such that they support only the TM_0 surface mode, metallization and feeding structures will also affect the structure's mode properties. As we showed in Chapter 2, through full wave eigenmode simulations, a grounded dielectric substrate loaded with a square metallic patch supports two more bound modes, which have been ignored in literature, in addition to the expected TM_0 mode described above; where these two additional modes are due to patch metallization and they are effective at much lower frequencies than operating frequency region of the array that is being studied here. The situation is more complicated for composite substrates where the potential of excitation of substrate modes, leaky or bounded, is higher. A modal solution to the complete structure is essential. Therefore, we have considered the whole structure with all types of metallizations as we have characterized supported surface and leaky wave modes.

Leaky wave modes are just space harmonics or Floquet modes of a bounded surface wave mode. The only difference between introduced leaky wave modes and substrate surface wave modes is that the phase constant of leaky modes β_{lw} is smaller than the free space phase constant k_0. Therefore, while surface wave modes, whose propagation constants are $k_0 \leq \beta_{sw}$, are bounded to the substrate and not radiating any energy to the air medium, leaky waves on the other hand are radiative toward certain directions determined by their propagation constant.

4.1.3 Excitation of Substrate Modes

Even though surface and leaky modes properties are determined by the structure's material and geometry configurations, their excitation requires certain types of feeding mechanisms. We saw, in Chapter 2, that a square patch antenna on a grounded dielectric substrate supports a surface wave mode identically along the x- and y- directions since the radiating patch and substrate are square; however, excitation of these identical modes along different directions can be different, depending on the feeding or excitation mechanism, or array elements' polarization. As the array elements are excited, electric currents on the array elements, whose main task is to form the radiation, may excite surface and leaky waves modes along a specific direction, which will propagate in the array structure similar to the modes propagating in a waveguide.

Excitation of surface and leaky wave modes vary with scan angle or array element phase substantially as well. To explore excitation of substrate modes further, we used transmission setup as the one used in Chapter 2; however, here each element in the array is excited as shown

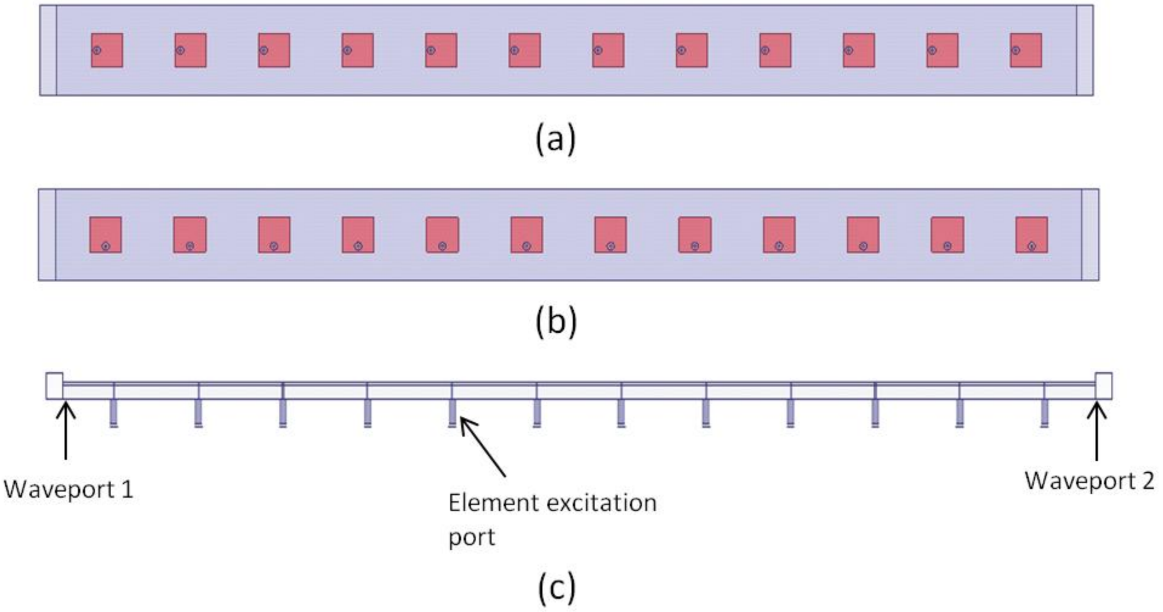

Figure 4.1 Transmission setup for demonstration of substrate wave modes excitation. (a) Top view E-plane, (b) top view H-plane, and (c) side view.

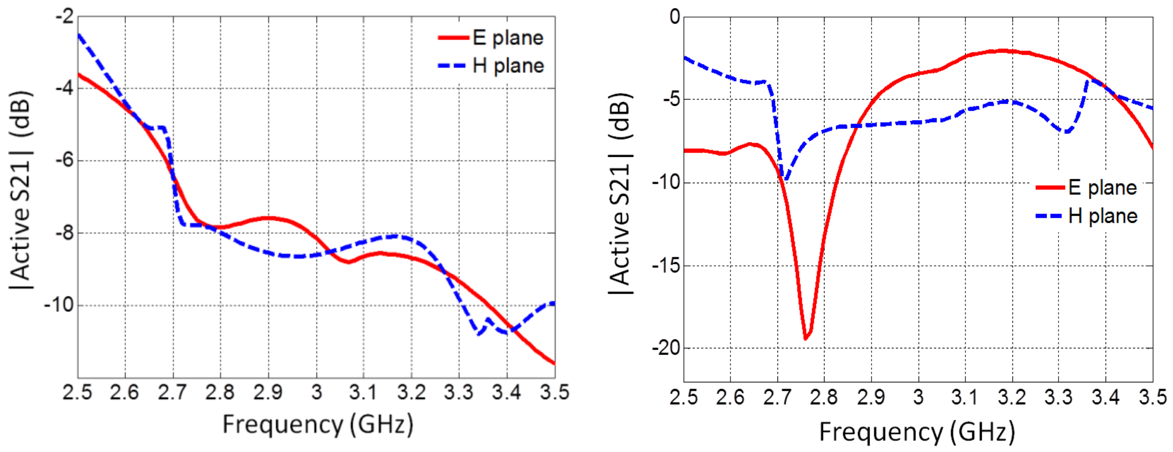

(a) (b)

Figure 4.2 Transmission through substrate when elements are (a) terminated with 50 Ω loads, (b) all elements are excited and phased for broadside radiation.

in Figure 4.1 and there are two additional ports at the edges to detect the waves propagating within the substrate, such as surface and leaky waves. Different cases are compared for the E- and H- scan planes in Figures 4.2 and 4.3. Note that these results are for a semi-infinite array of Figure 4.1, that is only 12 elements are used along the direction of propagation while an infinite number of elements are used along the other direction. In addition, analyses are performed within the -10 dB bandwidth of the radiating structure where it is from 2.70 to 3.01 GHz for an isolated single element, and from 2.80 to 3.11 GHz for the element in the planar infinite array environment of microstrip patch elements on a uniform grounded dielectric substrate. Therefore, we considered frequency regions between these two bands to analyze the semi-infinite structure in Figures 4.2 and 4.3.

We can observe, comparing Figures 4.2a and 4.2b, that substrate waves are effective even for broadside radiation. Excitation of array elements excites these substrate modes which propagate in the substrate. Since array currents are polarized along the E- scan plane, substrate modes are dominant along the E- plane as shown in Figure 4.2b. On the other hand when

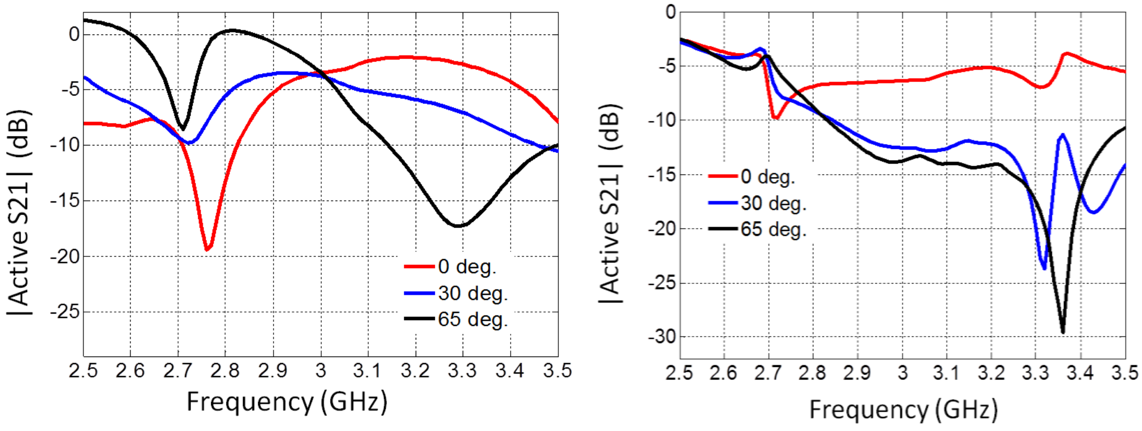

(a) (b)

Figure 4.3 Transmission through substrate when elements are phased for different scan directions in (a) E- and (b) H- scan planes.

elements are not excited, propagation within the substrate is similar along the E- and H- scan planes as illustrated in Figure 4.2a. However, our discussion is more accurate for the scan angles corresponding to phase matching condition between substrate waves and array modes, where excitation of substrate modes is the most significant; as shown in Figure 4.3a, propagation in the substrate peaks at these scan angles. For the array analyzed here, scan blindness occurs, as will be shown later, at 65° scan angle along the E- plane. The transmission results of Figure 4.3a agree well with this angle. On the other hand, this is not true, as expected, for the H- plane of Figure 4.3b where excitation of substrate modes is not achieved mostly due to array element current polarizations to be along the E- plane.

4.1.4 Scan Blindness

It is clear now that excited array structure can support two different modal mechanisms which are based on different roots and should not be confused. From another point of view, we introduced two different sets of Floquet modes; one represents the array field and the other represents the surface wave mode field, and it is possible that Floquet modes from these two different sets couple to each other. If that is the case, excitation of the substrate modes peaks and significant portion or all of the array energy couples to these modes and remains in the substrate instead of being radiated into the air. This happens as tangential phase constant of a radiation Floquet mode k_{pq} equals to that of a substrate mode β_{sub}. At the end, excitation of the substrate mode occurs in the same direction as the antenna element current direction. This coherent coupling or scan blindness condition can also be written as

$$\beta_{sub}^2 = \left(\frac{2\pi p}{d_x} + k_0 \sin\theta \cos\varphi \right)^2 + \left(\frac{2\pi q}{d_y} + k_0 \sin\theta \sin\varphi \right)^2 , \qquad (4.5)$$

where β_{sub} can be β_{sw} or β_{lw}, depending on the mode type under consideration. (4.5) is not a sufficient condition for scan blindness to occur; it is also needed that there is current, with proper polarization, available on the array structure to excite surface wave modes, which will have the same polarization as the excitation current; therefore, surface wave modes are more significant along the E-plane of microstrip arrays as shown in Figures 4.1-4.3.

Scan blindness phase matching condition (4.5) cannot be satisfied between bounded surface wave modes, whose phase constant β_{sw} is larger than that of free space k_0 and the $(0,0)$ Floquet mode or main beam; in most practical cases blindness is due to coupling between a surface wave mode and the $(\pm 1,0)$ Floquet modes. However, we can also observe, from (4.5), for the first time that scan blindness due to the $(0,0)$ Floquet mode or main beam is possible if the array excites leaky wave modes, whose phase constant β_{lw} is smaller than that of free space k_0. This condition has never been considered in the open literature, according to our best knowledge. However its impact is important especially for the modern integrated structures using composite substrates where the potential of leaky waves is greater.

As it is seen from (4.5) element spacing has a significant impact on scan blindness while substrate thickness and dielectric constant also have an impact indirectly through the substrate mode phase constant. For scan blindness analyses, it is desired to have blindness angle in the visible range and closer to the broadside direction. Even though increasing substrate thickness and permittivity forces substrate wave effects and scan blindness to the broadside, element spacing is the most significant parameter on the blindness angle. It is possible to have blindness close to the broadside for element spacing larger than half wavelengths, but that large element spacing also introduces grating lobes into the visible space. Therefore, for scanning arrays the element spacing is generally limited to half wavelength at the operating frequency. In addition, one of the main requirements of the whole structure eigenmode analysis, performed in Chapter 2, is that element spacing must be smaller than half wavelength at the array operating frequency. Scan blindness angle, on the other hand, is too sensitive to the element spacing, it approaches to the endfire direction and then disappears from the visible angle range, as shown in Figure 4.4, with decreasing element spacing and this makes analysis of scan blindness difficult. Considering an E-plane scanning array with only the first order $(1,0)$ Floquet mode, the scan blindness angle can be derived from (4.5) as

$$\theta_{sb} = \sin^{-1}\left(\left|\frac{\beta_{sub}}{k_0} - \frac{\lambda_0}{d_{x,y}}\right|\right). \tag{4.6}$$

Element spacing must be chosen close to the half wavelength for a straightforward blindness analysis. To induce scan blindness at smaller angles (closer to the broadside), substrate thickness and dielectric constant should also be chosen large, this helps to capture substrate modes

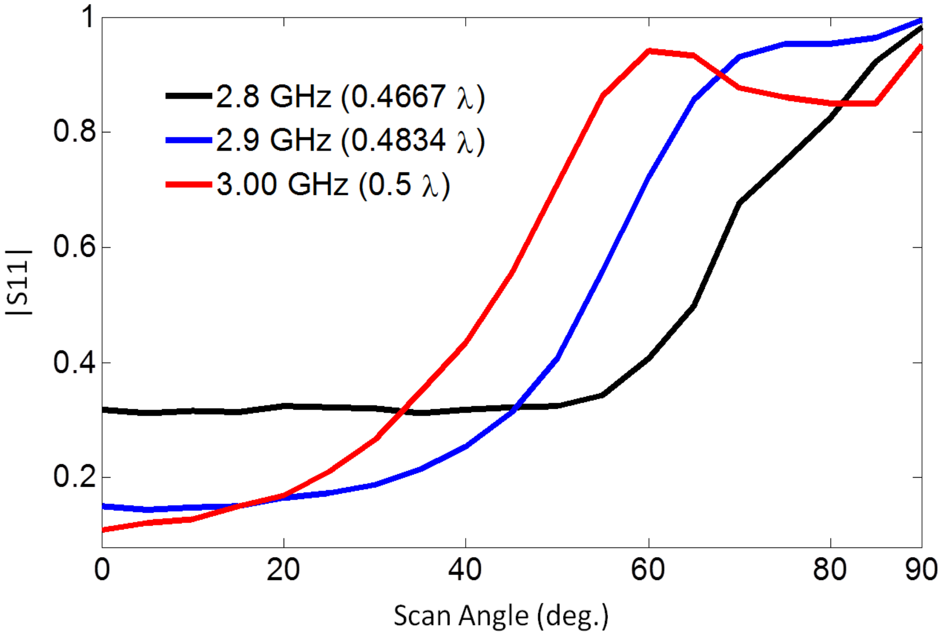

Figure 4.4 Element spacing effect on scan blindness. λ is free space wavelength at array operating frequency.

inducing blindness with eigenmode analysis since we cannot increase element spacing more. The array we will introduced further here has same substrate properties as the one used in the previous chapters. Note the scan blindness angle varies with the scan angle as well, or saying it in another way, blindness is dominant at certain scan angles but it occurs at nearby angles also.

4.2 Broadside Analysis

We saw how scan blindness makes phased array dysfunctional, and the elimination of scan blindness is therefore needed, which is the main objective of this thesis. The bandgap structure analyzed in the previous chapters is a good candidate for this since it provides both radiation and bandgap properties simultaneously. Before introducing scan blindness elimination using the proposed bandgap-antenna structure, here we first analyze the frequency response of this structure and that of an array on a uniform substrate at the broadside direction. Figures 4.5 and 4.6 show that the frequency behavior of an isolated antenna element may change remarkably when it is placed into an array environment, due to propagating substrate waves which couple array elements. Both input reflection coefficient and realized gain changes are greater for the

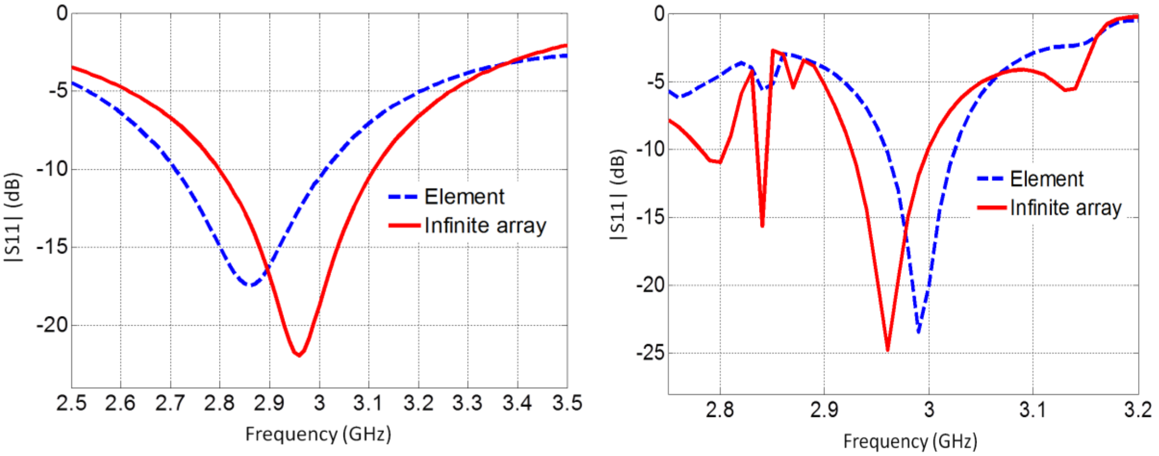

(a) (b)

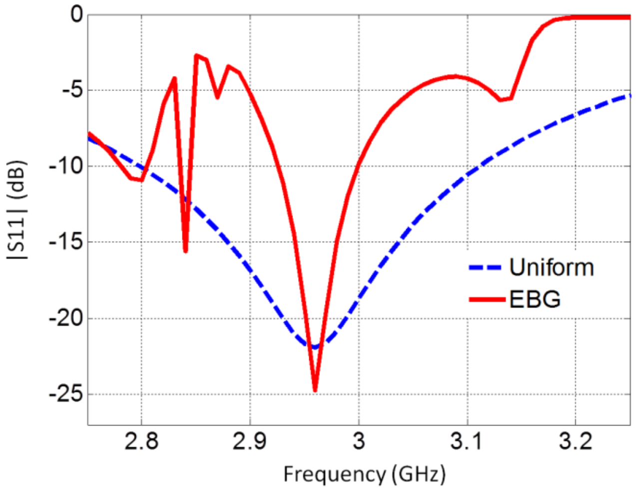

(c)

Figure 4.5 Input reflection coefficient for different cases. (a) Uniform substrate element vs. infinite array, (b) bandgap substrate element vs. infinite array, (c) Infinite array uniform vs. bandgap substrates.

case of uniform substrate than the case of the bandgap structure because of the presence of substrate modes in the uniform substrate. A slight change in the case of the bandgap structure is due to smaller computational size, per unit cell, for the infinite array, where the effect of space waves is more significant on the coupling between the elements; of course this effect is present

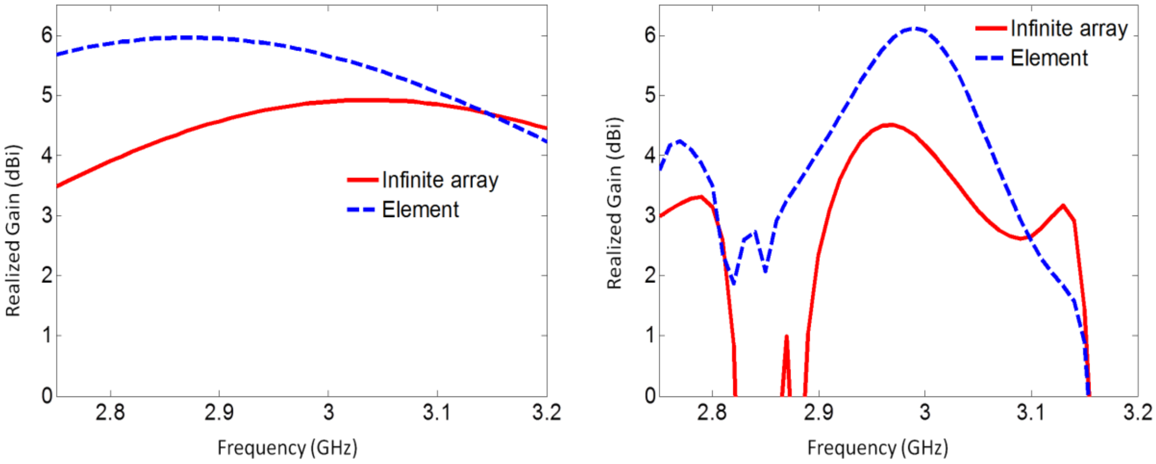

(a) (b)

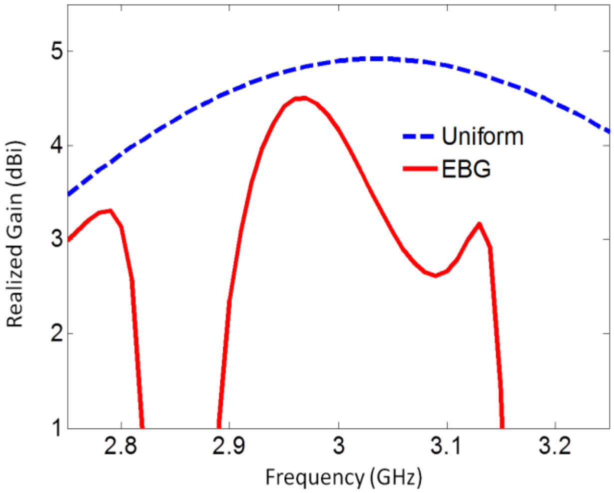

(c)

Figure 4.6 Realized gain for different cases. (a) Uniform substrate element vs. infinite array, (b) bandgap substrate element vs. infinite array, (c) Infinite array uniform vs. bandgap substrates.

for the uniform substrate arrays also but the substrate modes effect is more dramatic there. As shown in Figures 4.5c and 4.6c the uniform substrate array provides better reflection coefficient characteristics and realized gain over the frequency band of interest at the broadside radiation direction. The role of the bandgap array however is coming into the play as we scan the beam; as we will see, a complete elimination of scan blindness can be achieved with the bandgap arrays while an array of uniform substrate cannot function after certain scan angle, coinciding with the blind angle, which is 65° here.

4.3 Scan Analysis

Comparing to conventional bandgap approaches for the scan blindness elimination, the structure presented here provides better improvement because here the whole structure, which is co-designed for its radiation and bandgap characteristics, is a bandgap structure; while for the conventional solutions, bandgap unit elements were embedded into the array elements and usually bandgap elements were separated from the array element traces to protect their bandgap properties, by reducing couplings, so that only few bandgap rows could have been achieved. Therefore, substrate modes suppression is not complete; in addition, leaky wave suppression has never been investigated in the previous approaches in the context of the scan blindness elimination. On the other hand, the radiating-bandgap structure of this paper can be considered as a unit cell of a conventional bandgap material; but with the improvements of its radiating to broadside as an antenna element and suppressing leaky waves characteristics.

The radiating-bandgap structure can eliminate scan blindness along all scan directions due to its omnidirectional mode free bandgap behavior. Omnidirectional bandgap is essential for planar arrays, otherwise coupling, and hence scan blindness, would occur along some directions. Square shaped patch and rotational symmetric rings and via configurations make the omnidirectional bandgap possible with the proposed structure as we saw in Chapter 2; here

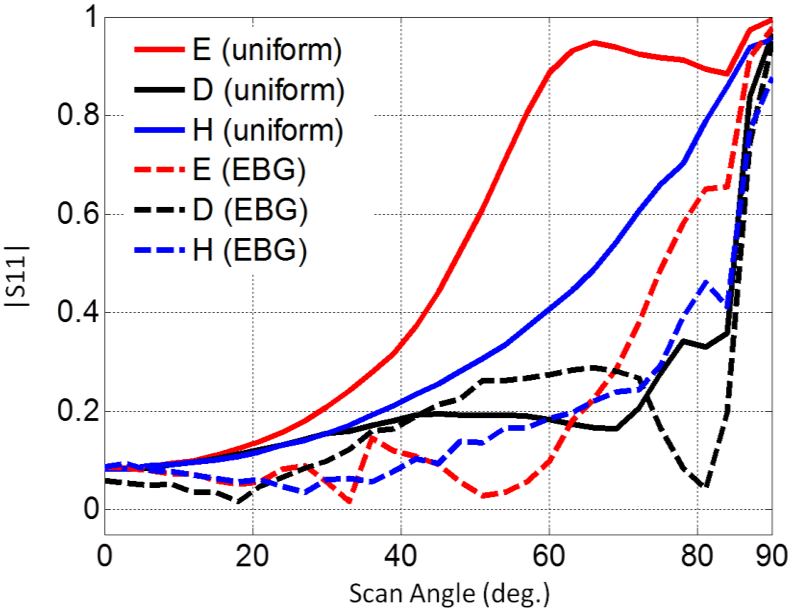

Figure 4.7 Scan behavior of uniform-substrate and bandgap-antenna arrays for different scan planes. Frequency is 2.96 GHz, element spacing is $(0.4933\lambda_0)$ and substrate thickness is $(0.0689\lambda_0)$.

we show the effect of this bandgap behavior on the array scan blindness elimination in Figure 4.7, where scan behavior of the uniform and the proposed bandgap structure are compared; the performance of the bandgap structure is obvious, scan blindness is completely eliminated from all scan planes. The most significant improvement is seen in the E- scan plane where the reflection coefficient is reduced from 0.946 to 0.181 at a scan angle of 65°, which coincides with the uniform array scan blindness angle. For all three scan planes shown in Figure 4.7, the reflection coefficient remains below 0.3 or -10 dB up to 70°. A slight increment in the D- plane is likely due to coupling between metallic parts of the unit element. In order to analyze the bandgap structure's scan blindness elimination performance we have chosen the size of the square substrate as 50 mm $\left(0.4933\lambda_0\right)$ and the substrate thickness is 6.985 mm $(0.0689\lambda_0)$, λ_0 is wavelength at the array operating frequency 2.96 GHz.

The design approach, co- designing of radiating and bandgap structures, can be applied to more compact arrays with smaller element spacing, where coupling between arrays increases.

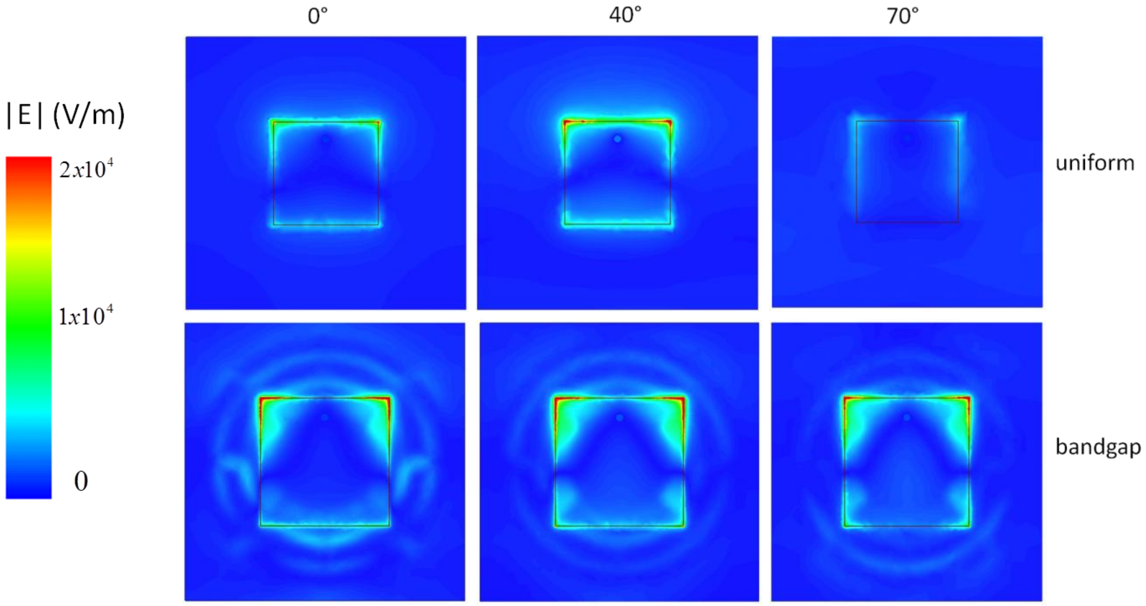

Figure 4.8 Electric field distribution on substrate surfaces of uniform-substrate and bandgap-antenna arrays for different scan angles: 0°, 40°, and 70° from left to right in the E- plane.

Indeed, bandgap characterization of more compact arrays is easier since the modal approach, as discussed in Chapter 2, is limited to the maximum element spacing of $0.5\lambda_0$.

To explore the performance of the radiating-bandgap structure further, we compared the magnitude of the electric field distributed over the substrate surface of the uniform and radiating-bandgap structures in Figure 4.8. Results indicate that for the case of the uniform arrays, radiation efficiency decreases by increasing the scan angle as the electric field is more concentrated near the patches at broadside, and finally patch elements cannot radiate when scan angle is in the range of the blindness angles as shown in the figure for scan angle 70°; one may think that observation of low field magnitude at this angle conflicts with our claim stated before: substrate modes will be excited strongly at the blindness angle. Indeed, both are true; excited surface waves trap the energy which is supposed to be radiated and hence radiation efficiency becomes too low. Excited surface waves do not appear in Figure 4.8 for 70° scan angle because they returned back to the excitation port which can be considered as termination. If, for example, there were no port connected the structure, we would observe very strong fields in the same figure due to strongly excited substrate waves at same 70° angle. For the case of the bandgap-radiating structure, on the other hand, field distribution remains almost the same for all scan angles in the figure. These observations agree well with the scan results in Figure 4.7; both indicate that the bandgap-radiating structure eliminates scan blindness completely along all possible scan directions. While we saw above that the uniform array has better broadside performance, it is not an efficient choice for beam steering applications mainly due to scan blindness, where the bandgap-radiating array has significantly improved scan performance over the uniform array.

Composite substrates contain metallization for different purposes and all these inclusions affect radiating structures' input impedance. In order to achieve impedance matching at the elements input, matching networks are the choice of the solution. As analyzed in the previous chapter, we also used matching network in our structure. Even though matching networks should electrically be isolated from the composite array elements, an inappropriately designed matching network can provide misleading results. As a reference, here in Figure 4.9, we report the effect of a matching network on scan blindness. Infinite array of microstrip patches on a uniform substrate, with the parameters shown in the caption of the figure, without matching network resonates at center frequency 2.72 GHz. We then matched the input impedance of this array measured at 3.00 GHz to 50 Ω; and both arrays, with and without matching network, are scanned at the same frequency 3.00 GHz. As expected, both arrays have scan blindness at the same angle, starting at 70°. As a result, a well designed matching network is not expected to affect array scan characteristics.

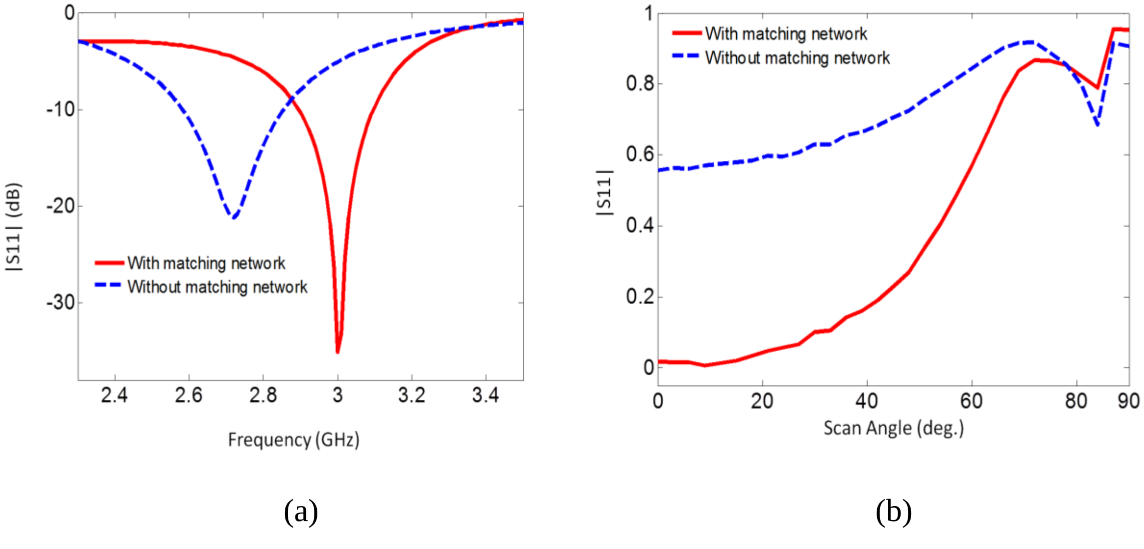

(a) (b)

Figure 4.9 Matching network effect on scan blindness for an array on uniform substrate. Dielectric constant is 4.5 and substrate thickness is 6 mm, substrate size is 50 mm (square). (a) S11 versus frequency, (b) scan behavior at 3 GHz.

4.4 Unit Cell Coupling Analysis

The bandgap-antenna structure is composed of multiple metallic layers, and couplings occur between these layers along the normal direction to the structure surface. These affect the structure's performance tremendously. Since the structure has been co-designed for bandgap and radiation purposes, internal coupling effects may be different on the bandgap and radiation properties. We investigated several different configurations which provided even better bandgap performance than the structure studied here; however, all of those structures failed when they were considered for the radiation and scanning analyses.

Another degree of internal coupling, which can be more severe and unpredictable at the first design scale, is that in order to scan the beam, element excitation phases are changed and this phase change will introduce unpredictable couplings varying with scan angles. On the other hand, internal coupling effects may not be that effective for broadside arrays since there is no phase change; thus, the design methodology presented here can be easily applied to broadside

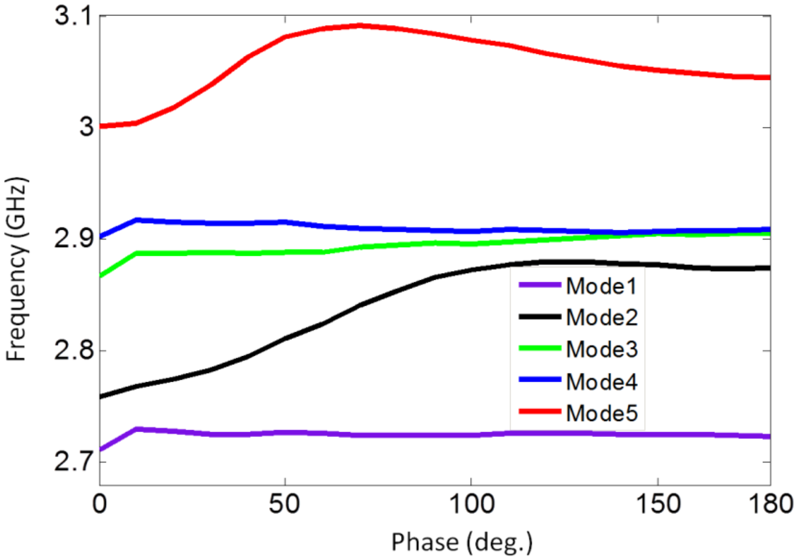

Figure 4.10 X-M section of the dispersion diagram of the unoptimized structure for the internal couplings analysis.

arrays for mutual coupling reduction, especially for highly integrated or compact arrays. Overall, consideration of the internal coupling effects is a key step of the design of the radiating-bandgap structure; it is as important as the modal analyses of Chapter 2 and scan blindness analysis of this chapter.

In order to explore the internal couplings further, we considered a structure with two layers of concentric rings and a top square patch, similar to the one presented in Chapter 2; this structure, however, has no cuts on its rings, and rings internal radii and widths are (mm): 10, 14, 20 and 3.4, 5.4, 3.00 respectively. The substrate material is a 3 mm of grounded dielectric with permittivity of 2.94 and above this dielectric layer there is another 3 mm dielectric layer with permittivity of 6.00. The bottom ring layer is on top of first dielectric layer and top ring layer is 1.00 mm away, underneath, from the top radiating patch, which is 25 mm in a square shape and fed 5.5 mm away from its edge by a coaxial probe; and the structure does not contain any vias. As shown in Figure 4.10, this structure has a bandgap from 2.92 to 3.00 GHz; having a bandgap

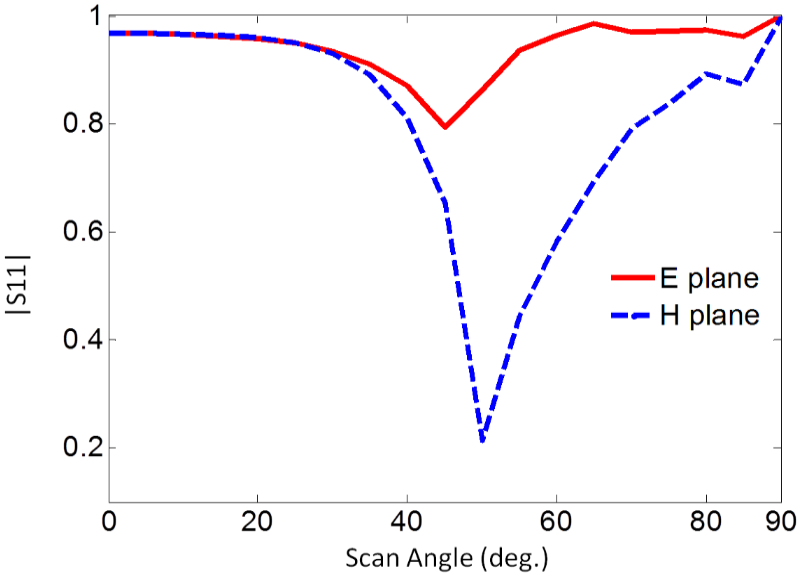

Figure 4.11 Effect of internal couplings to the scan behaviors for unoptimized structure.

around the desired array frequency with reasonable structure size is however not sufficient to appreciate the structure for scan blindness elimination, mainly due to the fact that its scan properties change with scan angles or excitation phase as shown in Figure 4.11. In the H- scan plane reflection coefficient deviates from its broadside values remarkably around scan angle 55°, if this structure would be matched at the broadside, there would be a peak in its reflection

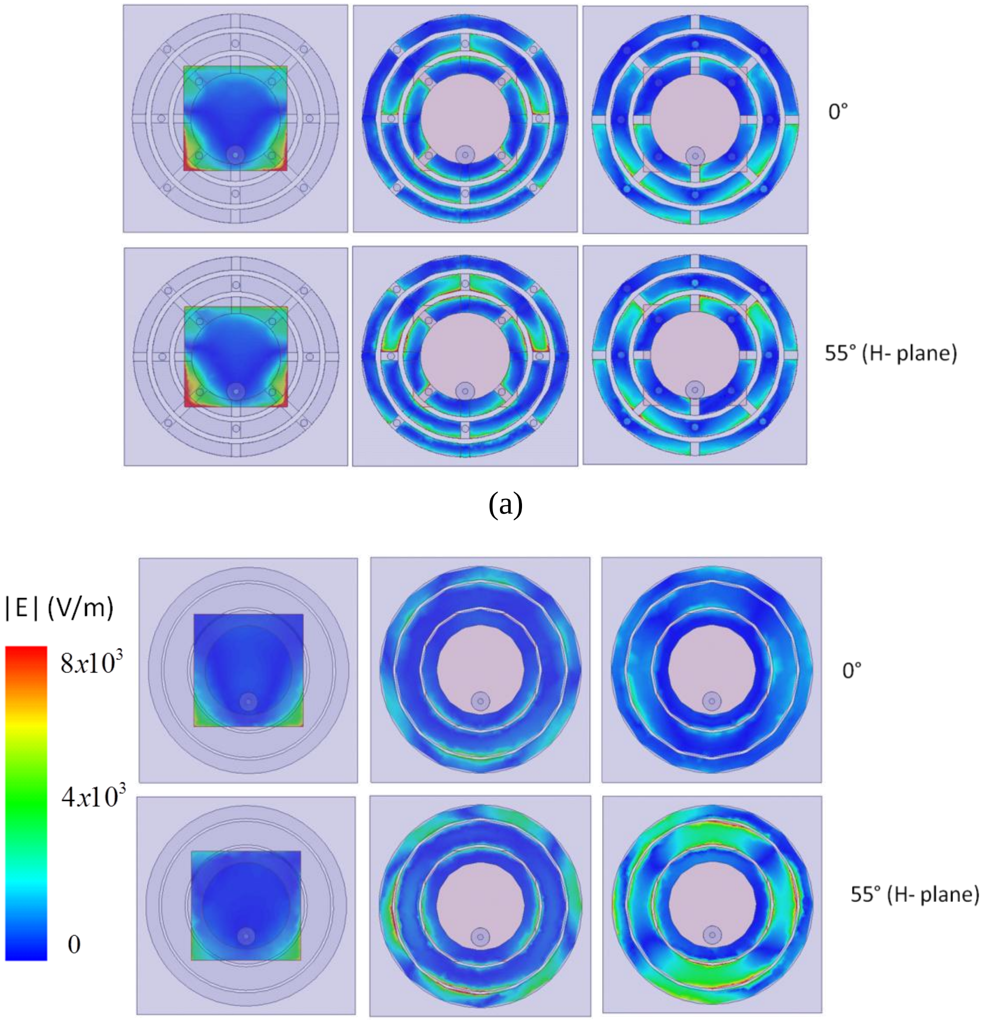

(a)

(b)

Figure 4.12 Visualization of internal couplings change with scan angle, (a) optimized structure and (b) unoptimized structure field distribution. From left to right: top patch - top ring layer - bottom ring layer.

coefficient at this angle 55° on the same scan plane, H-plane, so that overall effect would be like a scan blindness, at even smaller scan angles comparing to the real scan blindness angle. That is, internal couplings introduce scan blindness-like effect.

Effect of element phase on the internal couplings is visualised in Figure 4.12, where the electric field distributions on the radiating top patch, top layer rings, and bottom layer rings, from left to right, are shown. Figures 4.12a and 4.12b are for optimized and unoptimized, in terms of internal coupling reduction, structures. In particular, structure of Figure 4.12a is the one that has been studied throughout this thesis, while that of Figure 4.12b is the one just described above that has no cuts on its rings and has no vias. The electric field distribution remains almost the same over the optimized metallic parts for two different scan angles 0° and 55°, while the electric field is stronger at scan angle 55° than scan angle 0° over the concentric rings of the unoptimized structure in Figure 4.12b, where most of the energy couples to the lower ring layer; and these results agree well with reflection coefficient variation with scan angle in Figure 4.11 where the reflection coefficient decreases significantly at scan angle 55° because energy couples to the rings but not returning back to the port. This makes the reflection coefficient small but that does not mean that the structure is radiating efficiently at this angle. It is important to realize that internal couplings focused here are effective along the normal directions, coupling between different metallic layers, so that eigenmode analysis, which is for lateral propagation directions, cannot capture them as a valid mode.

4.5 Conclusion

Possible electromagnetic modes available in phased array structures have been detailed; these are related to array radiation or array structure. Then, the condition for excitation of structural modes, also known as substrate modes, and the dramatic result of coherent coupling between radiation and structural modes, known as scan blindness, were analyzed. The scan blindness problem from planar microstrip arrays has been solved by using the bandgap-antenna structure as a phased array antenna element. Internal electromagnetic couplings within the bandgap-antenna unit cell varies with element excitation phase or scan angle, and thus the ultimate structure of the bandgap-antenna structure has been optimized considering these internal couplings as well.

Chapter 5

Scan Analysis of Finite Arrays and Experimental Demonstration of Bandgap-Antenna Structure

Demonstration of scan blindness and the required technology for its elimination requires large number of antenna elements. The alternative way of a standard waveguide simulator, which is generally used to characterize printed arrays' scan behavior in the H- plane, is not applicable in the case of scan blindness analysis of microstrip patch arrays studied here, since these practical arrays have scan blindness in their E- plane. Therefore, we used finite arrays, both planar and linear configurations were considered, to characterize the radiating-bandgap structure performance for scan blindness elimination. Finite array designs were carried out using periodic domain decomposition method (available in HFSS) where meshes are generated for only one array element and the same meshes are then used for the other array elements. This method reduce memory requirement substantially for the finite array analysis. Analyzed uniform substrate and bandgap structure with stripline matching networks are the same as the ones studied in the previous chapters.

For experimental purposes, it is desired to have an array configuration with a minimum possible number of antenna elements. Uniform substrate array configuration should be determined such that the number of array elements is sufficient to detect scan blindness. Another important aspect of the finite array, besides the number of array elements, is the feeding network for beam scanning, which contains phase shifters and power dividers. However, it is still possible to characterize array scan behavior without using the feeding networks, but by using an active element pattern (AEP) and active reflection coefficient [48], where they refer to the pattern and reflection coefficient of the center element when only the center element is excited but all other array elements are terminated with 50 Ω. Therefore, here our objective is to analyze scan blindness with a minimum possible array elements without using phasing network mechanisms.

5.1 Array Size Analysis

In order to analyze the number of array elements for scan blindness detection, linear and planar array configurations of different sizes are considered in Figure 5.1a, where scan blindness of the same element in an infinite array shows scan blindness in the E- scan plane at 65° as discussed in the previous chapter. We can observe, from the AEP, that scan blindness is more effective in planar arrays and also it becomes more severe as the number of array elements is increased.

Since planar arrays with a large number of antenna elements are difficult to simulate and fabricate, we will look for the scan blindness effect from linear arrays with a minimum possible

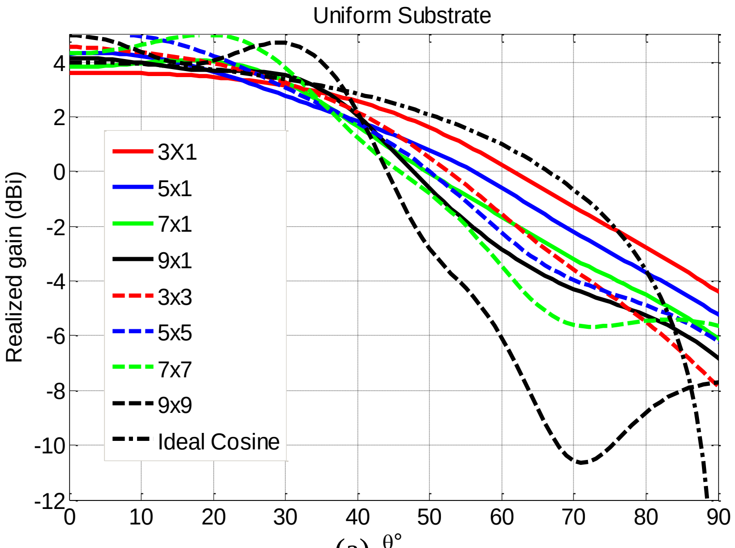

(a)

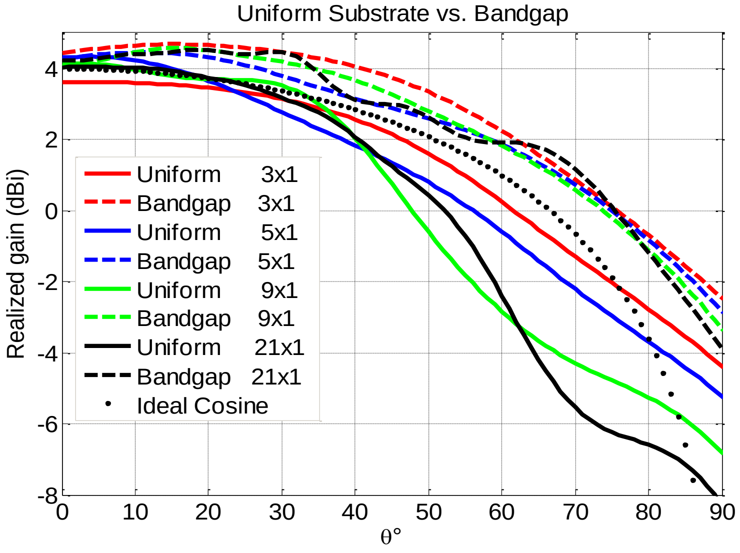

(b)

Figure 5.1 E-plane active element pattern for different array configurations, (a) uniform substrate planar versus linear arrays, (b) uniform substrate versus bandgap structure linear arrays.

of number antennas. As shown in Figure 5.1b, linear arrays still show blindness effect and it becomes more dominant with array size; more importantly, linear arrays of the bandgap structure demonstrate their successful elimination of blindness where it does not matter what array size is used for the bandgap arrays; AEP patterns of different size bandgap structures are almost the same and improve scan behavior substantially from the uniform array configurations.

In addition to the radiation consideration of the AEP of Figure 5.1, scan blindness can also be analyzed through the array elements input reflection coefficient while the array is fully excited. This case is similar to the infinite array of the previous chapter, where array scan blindness was characterized using the input reflection coefficient when all array elements are excited.

In the following, the active input reflection coefficient of the center element is used for the analyses. Since we do not use phasing networks and power dividers, an alternative approach of obtaining the center element active reflection coefficient, which changes with scan angle, is used. For that, mutual coupling between the center element and all the other elements is first obtained and then the corresponding active reflection coefficient of the center element is calculated as

$$S_n^{active} = \sum_{m=1}^{9} S_{nm}^{passive} e^{jk_0 d_x \sin(\theta_0)(n-m)}, \tag{5.1}$$

for linear arrays on the x-axis and with the element spacing of d_x; θ_0 is the scan angle along the E- plane. (5.1) can be modified and applied to planar arrays as well. Even though (5.1) is very useful for capturing array behavior without the use of the feed networks, it is limited to large-size arrays. That is, the finite array active reflection coefficient has a similar trend to that of the infinite arrays only up to some scan angles; at large scan angles, if the array size is not large enough, the active reflection coefficient drops significantly and detection of the blindness angle, if it is at these large angles, will not be successful [11-12]. For example, as we discussed in the previous chapter, the considered uniform infinite array has the scan blindness effective at 65°

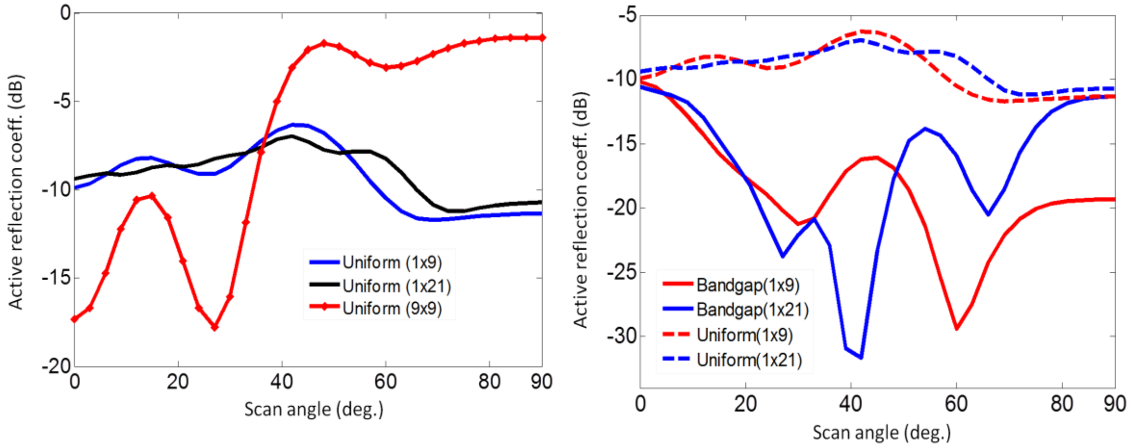

(a) (b)

Figure 5.2 Active reflection coefficient of the center element versus scan angle along the E- scan plane. (a) Different uniform substrate array configurations, (b) uniform substrate versus bandgap arrays.

and larger angles; however, as shown in Figure 5.2a, only the 9x9 array shows similar behavior to that of the infinite array. The other two 1x9 and 1x21 arrays active reflection coefficients drop after 50° and 60° scan angles so that they cannot detect the scan blindness by analyzing the active reflection coefficient of their center elements.

Comparing the bandgap and uniform arrays active reflection coefficients in Figure 5.2b, the bandgap arrays have smaller active reflection coefficients, which is reasonable. In fact, we expect, based on the case of infinite arrays of the previous chapter, that the bandgap arrays' input reflection coefficient to also approach unity toward the endfire direction; however they remain below -10 dB for the entire scan volume primarily due to the small array size.

Based on the AEP and active reflection coefficient analyses, we can see that it is more practical to analyze scan blindness, for the microstrip patch arrays, and characterize the bandgap structure by using radiation instead of the input reflection coefficient. Note that the case can be different for different element types, as waveguide simulator can measure dipole elements input reflection coefficients as shown in [26].

5.2 Finite Array Radiation Characterization

The radiation behavior of a fully excited array, at different scan angles or excitation phases, is of the primary interest. Note that phase shifters and power dividers will not be used for the array under investigation here. Instead, the complex-valued far fields of the array due to excitation of each individual element, while all the other elements are terminated with matched loads, are first obtained. Subsequently, the response of the fully excited array, as if the array was fed through the phase shifters and power dividers, can be found in [49] as

$$E^{array}(\theta,\phi)=\sum_{m=1}^{9}E_m^{element}(\theta,\phi)e^{j\alpha_m}e^{-jk_0 m d_x \sin(\theta)\cos(\phi)}, \tag{5.2}$$

where the generic excitation phase is represented by α_m. (5.2) basically states that the complex fields of a fully excited array consist of coherent summation of the elements' fields. After obtaining complex field data of the fully excited array, the realized gain, which accounts for mismatches at the elements inputs as well, can be determined from (5.2) as

$$Gain^{array}(\theta,\phi)=\frac{4\pi\left|E^{array}(\theta,\phi)\right|^2}{2\eta_0 P_{in}^{array}}, \tag{5.3}$$

where η_0 is the free space impedance, and P_{in}^{array} is the total input power to the array elements.

It is important to realize that both (5.2) and (5.3) can be applied to either co- or cross-polarized field components. In the case of the total array gain, the complex valued co- and cross-polarized field components are first added, and then the total array gain can be found from this total field. In our case, the array elements are fed along the x-axis and their surface currents are also polarized along the x-axis. In addition, we focus mainly to the E-plane for the scan blindness analysis. Therefore, according to Ludwig's third definition of cross-polarization, co- and cross-

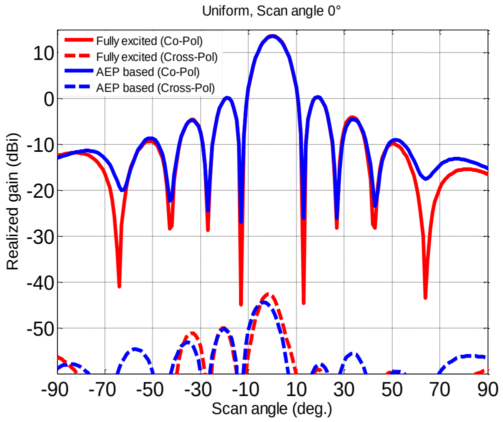

(a)

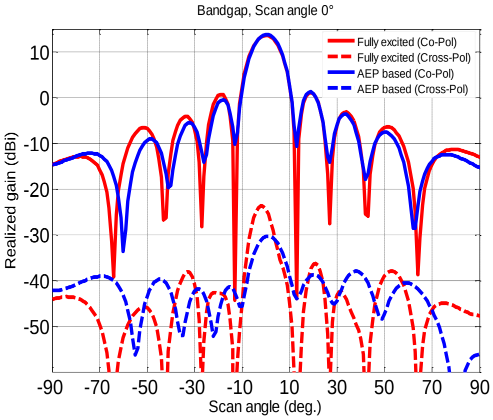

(e)

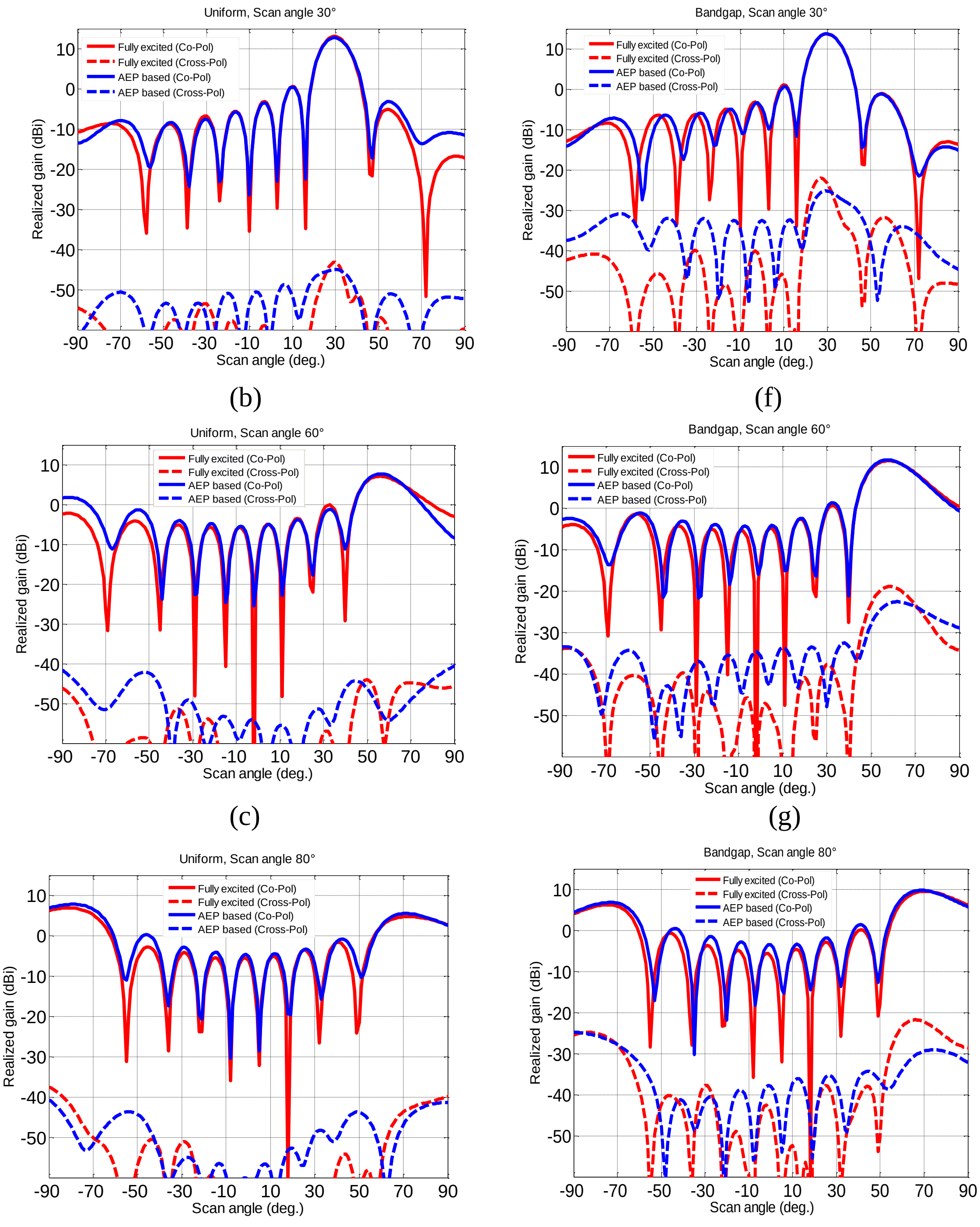

(b) (f)

(c) (g)

(d) (h)

Figure 5.3 E- plane co- and cross-polarization realized gain patterns, of fully excited arrays versus that of based on (2) and (3), for 1x9 uniform and bandgap arrays at different scan angles. (a)-(d) Uniform substrate for scan angles: 0°, 30° , 60° , 80° (e)-(h) bandgap structure for scan angles: 0°, 30° , 60° , 80°.

polarized field components of the array being analyzed here are

$$E_{co} = \left(E_\theta \cos(\phi) - E_\phi \sin(\phi)\right)\Big|_{\phi=0} = E_\theta, \tag{5.4}$$

$$E_{cross} = \left(E_\theta \sin(\phi) + E_\phi \cos(\phi)\right)\Big|_{\phi=0} = E_\phi, \tag{5.5}$$

As illustrated in Figure 5.3, the AEP based on (5.2) and (5.3) can capture array scan behavior accurately. The fully excited array is simulated in HFSS with progressive excitation phase between the elements, but not by using any phase shifting network, while the AEP based results were computed from (5.2) and (5.3) using AEPs of each element which were taken from the simulated array as only the respective array element was excited. The matching between the processed and the fully excited simulated arrays convinces us that we can obtain array scanning radiation characteristics experimentally without using any phase shifters or power dividers. In addition, if the array is large enough, the pattern of the center element suffices, which then will replace all the other element patterns in (5.2).

Another important observation in Figure 5.3 is that cross-polarization levels of the bandgap array are well below the co-polarization levels even at large scan angles. Even though the cross-polarization performance of the the bandgap array is slightly deteriorated with respect to that of the uniform array, it is still better than 30 dB at a scan angle of 80° or larger.

In order to illustrate the performance of the bandgap elements on the fully-excited array, co-polarized scan patterns of uniform and bandgap arrays, of 1x9 elements, are compared in Figure 5.4 at different scan angles. While their patterns overlap at the broadside direction, the effect of scan blindness becomes clear after the 60° scan angle. Indeed, scan blindness remains effective from around 60° to 90°. In particular, peak gain differences between these two arrays are 3.9 dBi and 4.3 dBi for the beams forced to point to 60° and 80° scan angle directions. This difference becomes larger and the performance of the bandgap array will become more appreciable as the element numbers are increased. It is also important to notice that patterns of both array configurations are similar; and therefore, the bandgap array can replace conventional microstrip arrays without any alterations on the beam qualities of the original array.

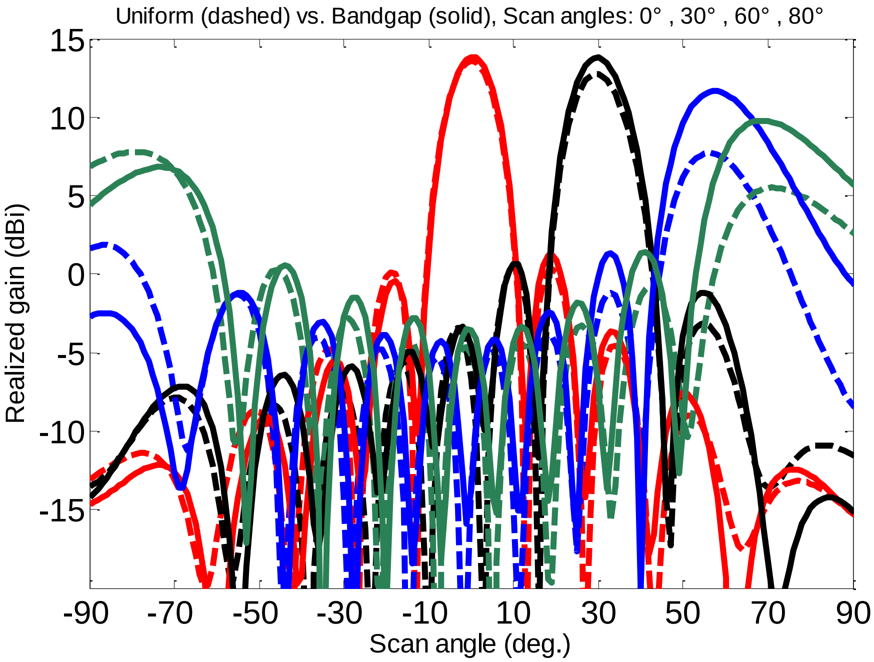

Figure 5.4 Fully-excited simulated E-plane co-polarized scan patterns of uniform and bandgap 1x9 arrays.

A more detailed comparison of the uniform and bandgap arrays is given in Figure 5.5, where realized gains of the corresponding arrays are compared at scan angles from broadside to endfire. In addition, the effect of the number of array elements is studied in order to emphasize improvements due to the use of bandgap arrays. At the broadside direction both arrays provide very close gain values, 13.55 versus 13.78 for 9 elements uniform and bandgap arrays, and 17.24 versus 17.46 for 21 elements uniform and bandgap arrays; however, as the arrays are scanned, the uniform array gain decreases significantly and deviates from the ideal scan values. The reduction, from the ideal values, is more significant around the blindness angles, i.e. between 60°

and 70°. On the other hand, the gain of the bandgap arrays remains higher than the ideal scan values for all scan directions. Both 9 and 21 element arrays demonstrate the bandgap effect , however the effect is clearer for the 21 element array. In particular, gain difference between the bandgap and uniform arrays is 4 dBi and 6 dBi at a scan angle of 70° for 9 and 21 elements arrays, respectively. For larger linear or planar arrays this difference becomes larger, where the actual role of the bandgap array shows up.

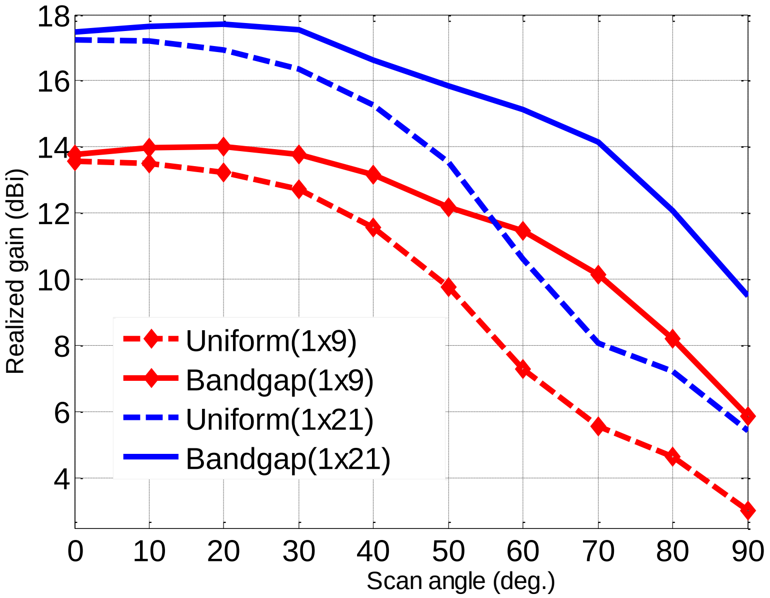

Figure 5.5 Realized gain versus scan angle for (a) 1x21 and (b) 1x9 linear arrays.

5.3 Experiment

5.3.1 Array Configuration

For experimental demonstration of the bandgap array, we considered the analyses of the previous sections. As such, we have chosen the smallest array size, which is a 1x3 linear array. As shown in Figure 5.1b, performance of the bandgap structure can be clearly demonstrated for the scan blindness elimination on this size of array. Another important point in the experimental work is to modify impedance matching network; previous analyses in this thesis were based on the a stripline matching network. However, it is very difficult to fabricate the bandgap structure with a stripline matching network due to vias within the stripline. Instead, an open stub microstrip line matching network has been used in the experimental prototype; the bandgap array

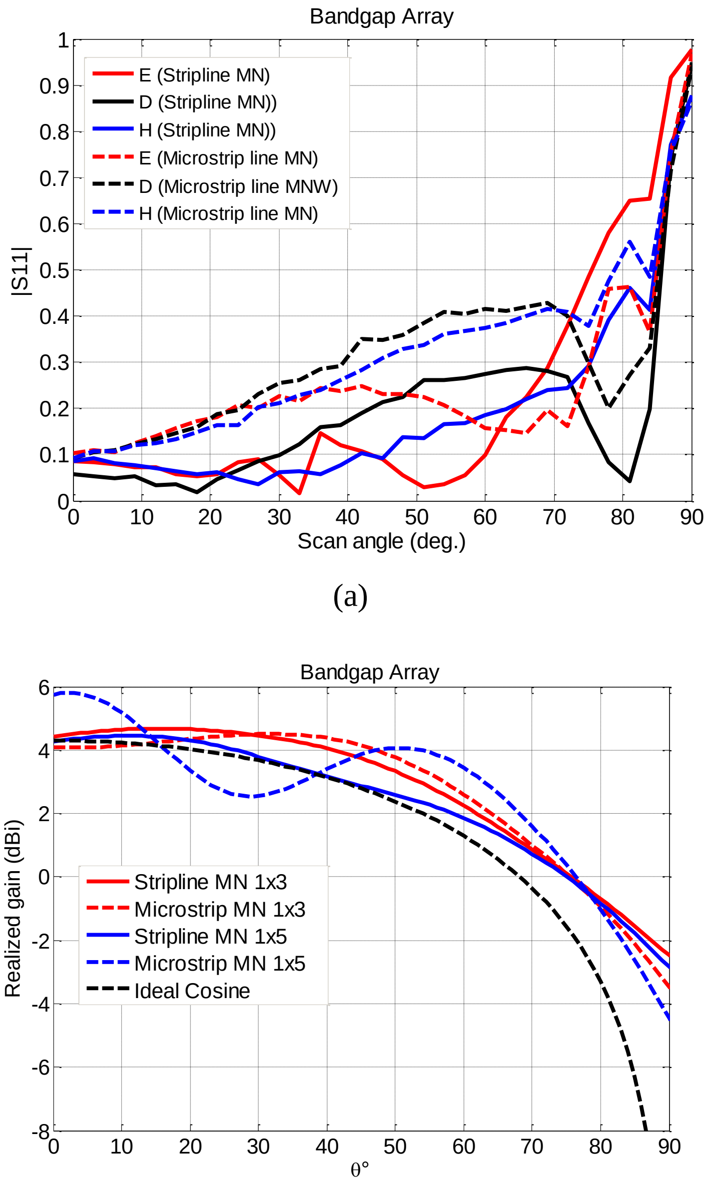

(a)

(b)

Figure 5.6 Comparison of bandgap arrays with stripline and microstrip line impedance matching networks. (a) Infinite array scan behavior, (b) active element patterns in finite arrays.

elements were fed through connectors to the CPW inputs, whereas uniform substrate array elements were fed through SMA probes directly.

A microstrip line matching network was designed such that couplings in the matching network are minimum, however the performance of the microstrip line matching network is still below that of the stripline matching network because there is no coupling in the stripline

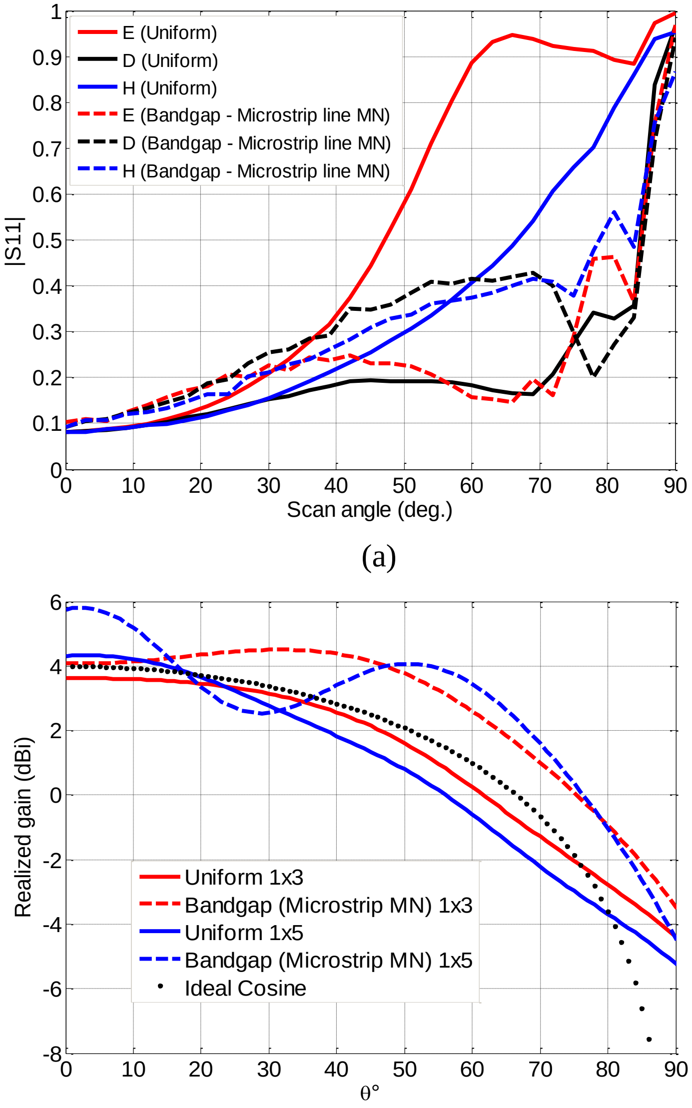

(a)

(b)

Figure 5.7 Microstrip line impedance matching network based bandgap array's performance for scan blindness elimination from the uniform substrate arrays. (a) Infinite array scan behavior, (b) active element pattern in finite arrays.

matching network due to fencing vias. Even though microstrip line matching network substrate is electrically very thin, $\varepsilon_r = 3.27$ and the thickness is 0.635 mm (operation frequency is 2.96 GHz), the open stub is long (20 mm) and that causes couplings and affects the overall array performance. Figures 5.6 compares the bandgap arrays with different matching networks, infinite array scan characteristic of the microstrip line based bandgap array is slightly deteriorated from that of the stripline one. For the finite array case, their active element patterns remain close to each other in 1x3 and 1x5 arrays; however 1x5 is oscillatory because of its larger size.

We further investigated performance of the bandgap array with microstrip line matching network for eliminating the scan blindness from the uniform substrate arrays in Figure 5.7. Infinite array eliminates the scan blindness from the most critical scan plane, E-; scan performance on the other planes is also successful even though slight increments, due to microstrip stub, can be observed as compared with that of the stripline array. For finite arrays couplings in matching network are less effective. As shown in Figure 5.7b finite, 1x3 and 1x5, bandgap arrays with microstrip line matching networks show clear performance enhancement over the uniform substrate arrays.

Overall, the smallest array size, 1x3, with a microstrip line matching network will be fabricated to demonstrate the bandgap array for the scan blindness elimination. Its performance will be compared with a fabricated uniform substrate array of the same size.

5.3.2 Fabrication

The fabrication process of the bandgap array is based on the conventional photolithography. Each layer of the structure shown in Figure 2.1 with microstripline impedance matching network

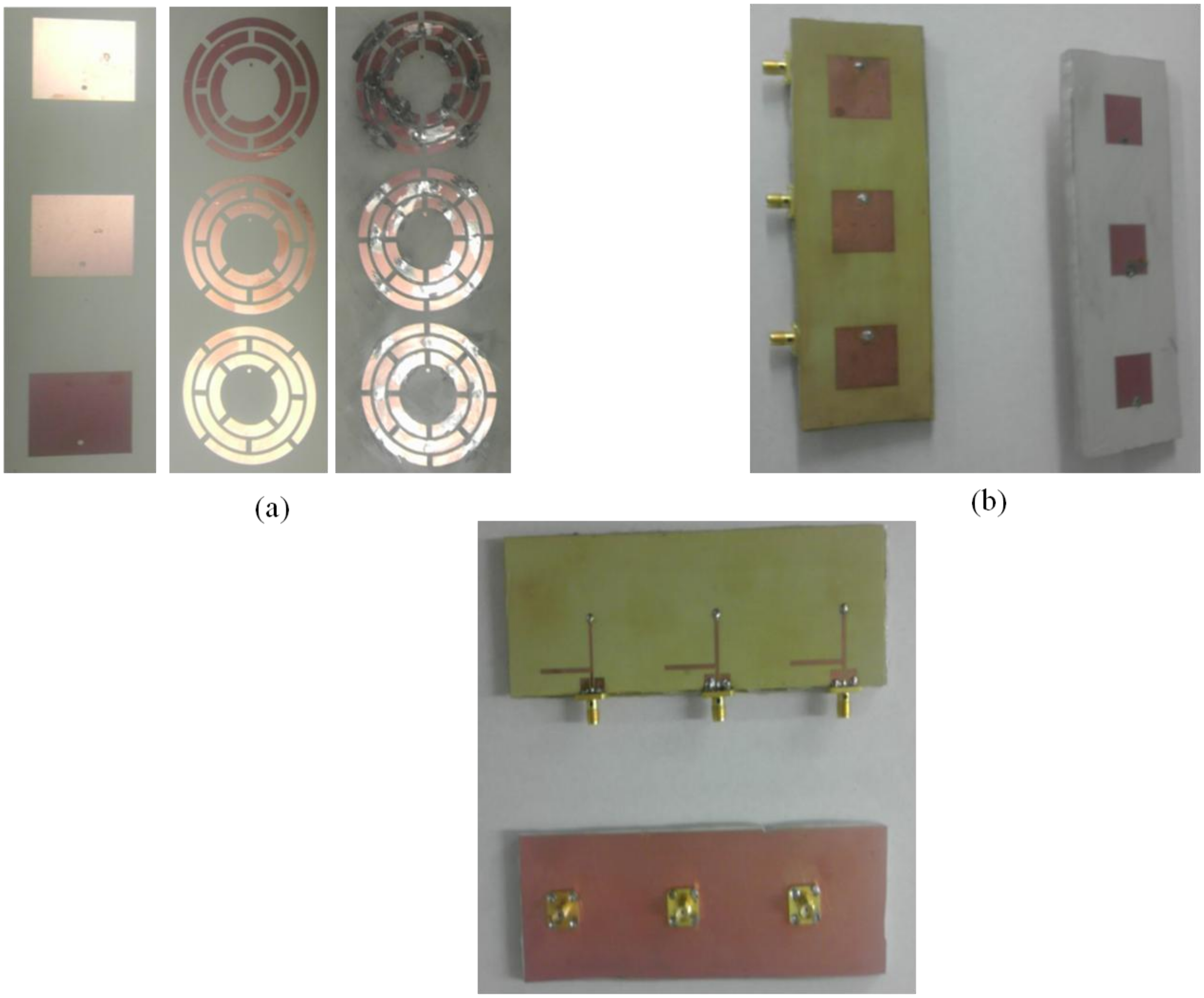
(a)
(b)
(c)

Figure 5.8. Fabricated bandgap and uniform substrate arrays. (a) Different layers of bandgap-antenna structure, (b) top and (c) bottom views of the uniform and bandgap arrays.

was first fabricated and then these layers were bonded together by using Rogers 3001 bonding film at 220°C temperature for about 30 minutes. The stacked materials were aligned and pressed before applying heat. The same size of the uniform substrate array was also fabricated to demonstrate the bandgap array performance enhancement. Copper wires are used as vias, which are soldered to the connected layers; since the stacked layers needs to be heated, the solder flows and disconnects layers that supposed to be connected with vias. Therefore, it is critical to not making soldered vias planar otherwise disconnection of layers will be more possible. The fabricated bandgap and uniform arrays are shown in Figure 5.8.

5.3.3 Experimental Results

Fabricated antenna arrays were measured in the UCI anechoic chamber; the measurement setup is shown in Figure 5.9. Arrays under the test were used as receiver antennas while a horn antenna was used as transmitter. The measured fabricated array results are shown Figures. 5.10 and 5.11, where only the center elements of the bandgap and uniform substrate arrays are excited while the other elements are terminated with 50 Ω loads. The bandgap array provides better impedance matching; however sharp two transitions, near 2.70 GHz frequency, do not mean the bandgap array radiates effectively as also discussed in chapter 3. But they are due to internal couplings and concentric ring shapes; that is, excited array energy remain between the metallic layers embedded within the substrate at these

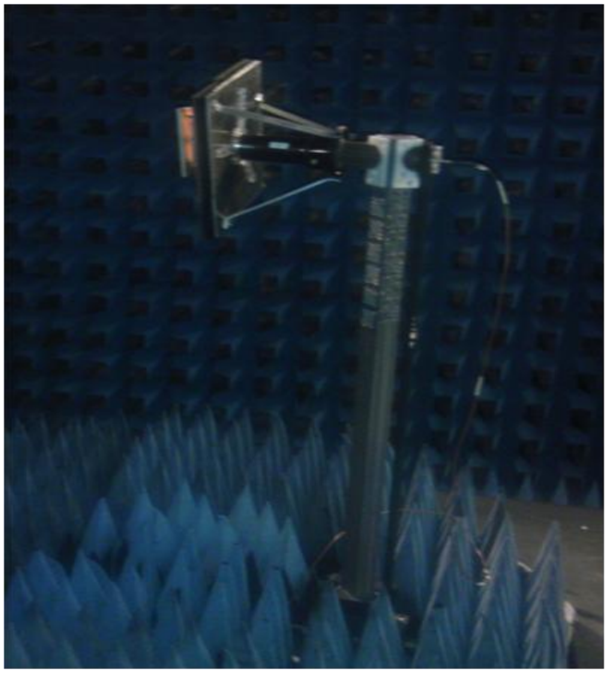

Figure 5.9. Fabricated array on the measurement setup in the anechoic chamber.

two deep peaks. However, it still have -10 dB impedance matching up to 2.95 GHz. Frequency bandwidth from 2.80 to 2.95 GHz can be used to characterize the bandgap array. Uniform array on the other hand has very narrow bandwidth of -10 dB centered at 2.77 GHz. For larger uniform arrays of the same one, -10 dB impedance bandwidth will shift upward in the frequency while that of the bandgap array will remain almost the same.

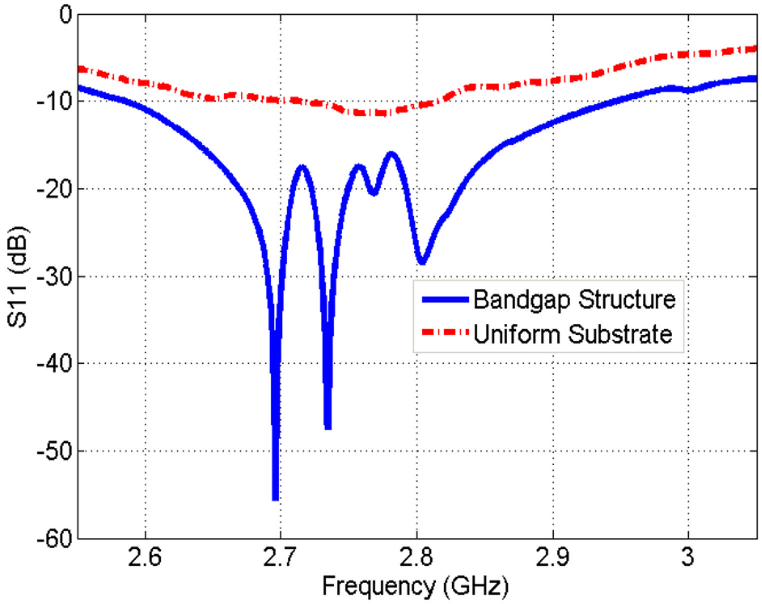

Figure 5.10. Input reflection coefficient of the center elements for the fabricated bandgap and uniform substrate arrays.

Radiation from the fabricated array prototypes were measured at frequency 2.94 GHz and is shown in Figure 5.11. Since our objective is to study the scan blindness effect, the chosen frequency for the array characterization, i.e. measuring the radiation, should be very close to the array half-wavelength (or unit element size) frequency, which is 3 GHz here. This analysis frequency was 2.96 GHz in the previous sections for the simulation based analyses. Effect of the bandgap on the elimination of the substrate waves is clear on the measured results also. The realized gain from the bandgap array remain higher than that of the uniform array along all the

visible scan angles. However, the gain difference between these two arrays along the positive scan directions is more and peaks, where the difference is close to 6 dBi, near the scan directions

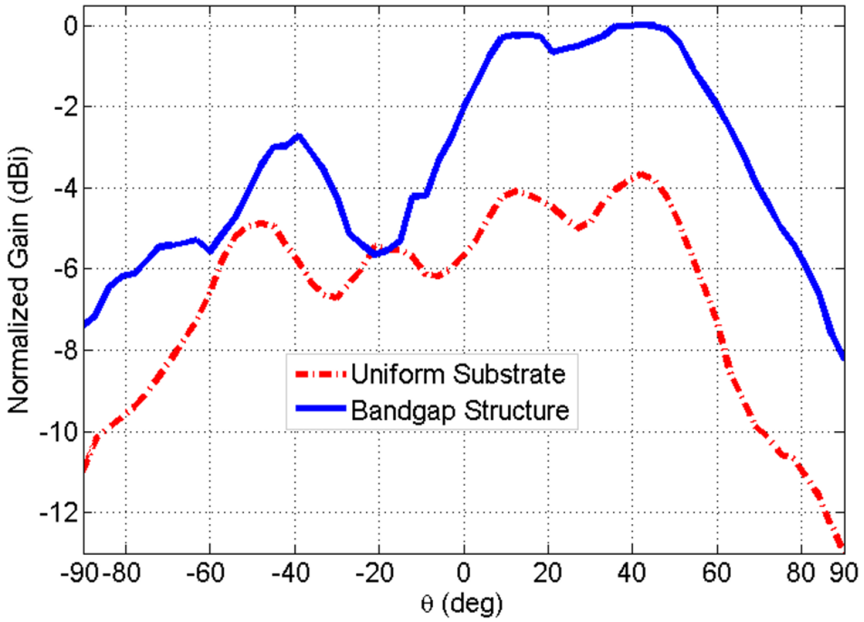

Figure 5.11. Normalized realized gain of the fabricated bandgap and uniform substrate arrays when only the center elements are excited or active element patterns.

bandgap on the elimination of the substrate waves is clear on the measured results also. The realized gain from the bandgap array remain higher than that of the uniform array along all the visible scan angles. However, the gain difference between these two arrays along the positive scan directions is more and peaks, where the difference is close to 6 dBi, near the scan directions corresponding to the scan blindness angle, which is 65° for the array have been studied here as also explained in the previous chapters. As a result, the scan blindness elimination capability of the bandgap-antenna arrays has been proved experimentally.

5.4 Conclusion

The scan blindness effect on the finite size phased arrays has been investigated in this chapter; array configurations and element numbers were found to be very effective on the scan blindness effect. Analysis of scan blindness can be performed from either array's radiation or input reflection coefficient. However, the input reflection coefficient requires a large numbers of elements in an array in order to detect scan blindness; on the other hand, very small arrays in both linear and planar configurations can show the scan blindness effect from their radiation behavior, such as active element pattern. Scan blindness elimination performance of the bandgap array has been detailed through the active element patterns and fully excited arrays. In addition, for scanning characterization, no phase shifter or power dividers were used; instead, individual elements complex field components were added and then the resulting field values were used to process the array radiation.

Finally, an optimum array configuration has been found for experiments. For that, the stripline impedance matching network of previous chapters has been replaced by a microstrip line impedance matching network for ease of fabrication. 1x3 linear array of the bandgap and uniform substrates were fabricated and measured, and performance of the bandgap array has been proved through scan blindness elimination or scan behavior enhancements.

Chapter 6

Conclusion

This thesis investigates microstrip phased arrays that are free of substrate waves. A novel design methodology has been proposed into the integration of phased arrays with electromagnetic bandgap materials. A multifunctional structure, which can radiate as a phased array element and function as a unit cell of a bandgap material simultaneously, has been designed, analyzed, fabricated, and measured. The proposed structure does not support any electromagnetic wave mode, e.g. surface or leaky waves, in the substrate or array structure along the lateral directions, therefore array characteristics are improved significantly. Specifically, fundamental problem, associated to all types planar phased arrays, of the scan blindness is resolved along all possible radiation directions.

Limitations of the previous efforts on the integration of planar phased arrays and electromagnetic bandgap materials are reviewed in Chapter 1, and the necessity of the multifunctional radiating bandgap structure, of this thesis, is emphasized.

Chapter 2 describes the unit cell of the radiating-bandgap structure, which has four metallic layers. Since the objective is to utilize the structure in planar array configurations, omnidirectional bandgap is essential part of the proposed structure. Metallic inclusions to the unit cell are concentric ring-shaped patches, vias which are configured as rotationally symmetric, and square-shaped top patch serving as a radiator; unit cell is also in a square shape. The structure is capable to provide omnidirectional bandgap. Bandgap has been investigated using

HFSS eigenmode solver and two port transmission setups. Even though two port transmission setup is valid only for on axis propagations, it has been used to investigate the role of the leaky waves, which are not stable in the eigenmode setup.

Radiation characteristics of the multifunctional radiating-bandgap structure have been studied in Chapter 3. The structure has been fed through a coax fed stripline impedance matching network. It has similar radiation characteristics, such as radiation pattern, polarization, and gain, as a conventional microstrip antenna. Stripline impedance matching network, which has fencing vias and isolate signal traces from any other couplings, has been chosen on purpose in order to focus on the bandgap structure's radiation behaviors only, but not the effect of radiations or couplings in the matching network itself.

Scanning performance of the infinite phased arrays based on the proposed structure has been investigated in Chapter 4. First, the role of both bound (surface) and radiating (leaky) substrate modes in the scan blindness has been detailed; composite substrates which has metallic inclusions potentially excites radiating substrate modes which also result in scan blindness. The proposed structure suppresses both types of substrates modes, therefore a complete elimination of scan blindness, along all directions, has been achieved. Coupling within a unit element of the radiating-bandgap structure has been analyzed using field distribution on the metallic surfaces at different scan angles or excitation phases; we found that having bandgap, which is necessary, does not guarantee that the array will be blindness free, mainly due to these internal couplings between different layers which cannot be detected through eigenmode analyses along the lateral directions.

In order to realize the array based on the proposed structure, we have analyzed different size arrays and compared with those on the uniform substrates in Chapter 5. Active element pattern and active reflection coefficient were analyzed to determine the proper array size for experimental demonstration. 3 element linear array prototypes of the uniform substrate and bandgap structure have been fabricated and comparisons of their active element patterns confirmed simulation results and elimination of scan blindness.

Future endeavors of this research has several different directions. First, a numerical mode solver is needed to capture higher order leaky modes properly since the available commercial solvers do not provide stable results for this task. Another improvement can be done on the geometrical modification of the presented structure, a planar structure without any vias would make the design and fabrication cycles easier and shorter. Moreover, fabrication of the proposed structure with stripline impedance matching network, where there are no couplings in matching network layer, would demonstrate actual performance of the radiating-bandgap structure. A physical model based on the lumped elements and multiconductor transmission lines can be developed for dispersion analyses and couplings between different layers. Also, the methodology presented in this research, co-designing of the bandgap and phased arrays structures, can be applied to other applications as well, such as mutual couplings from broadside arrays and microwave filters.

Bibliography

[1] R. E. Munson, "Conformal microstrip antennas and microstrip phased arrays", *IEEE Trans. Antennas Propagat.*, vol. AP-22, pp. 74-78, 1974.

[2] D. Sievenpiper, L. Zhang, R. F. J. Broas, N. G. Alexopoulos, and E. Yablonovitch, “High-impedance electromagnetic surfaces with a forbidden frequency band,” IEEE Trans. Microwave Theory and Techniques, vol. 47, pp. 2059–2074, Nov. 1999.

[3] A. Hewish, S. J. Bell, J. D. H. Pilkington, P. F. Scott, and R. A. Collins, "Observation of a rapidly pulsating radio source", Nature, 217; 709–713, 1968.

[4] Wikipedia. Phased Array. Available: http://en.wikipedia.org/wiki/Phased_array.

[5] A. Safaripour, S. M. Bowers, K. Dasgupta, and A. Hajimiri, "Dynamic polarization control of two-dimensional integrated phased arrays," IEEE Trans. Microwave Theory and Techniques, vol. 64, pp. 1066–1077, Apr. 2016.

[6] I. Gresham, A. Jenkins, R. Egri, C. Eswarappa, F. Kolak, R. Wohlert, J. Bennett, and J. P. Lanteri, "Ultra wide band 24GHz automotive radar front-end," in Microwave Symposium Digest, 2003 IEEE MTT-S International, 2003, pp. 369-372 vol.1.

[7] L. Qian, L. Qingming, and B. Chance,"2D phased array fluorescence wireless localizer in breast cancer detection," in Computer Architectures for Machine Perception, 2003 IEEE International Workshop on, 2004, pp. 71-73.

[8] C. A. Balanis, “Antenna Thoery: Analysis and Design,” Wiley, New York, 1997.

[9] D. M. Pozar and D. H. Schaubert, “Scan blindness in infinite phased arrays of printed dipoles,” IEEE Trans. Antennas Propagat., vol. 32, pp. 602–610, June 1984.

[10] D. M. Pozar and D. H. Schaubert, “Analysis of an infinite array of rectangular microstrip patches with idealized probe feeds,” IEEE Trans. Antennas Propagat., vol. 32, pp. 1101–1107, Oct. 1984.

[11] D. M. Pozar, “Analysis of finite phased arrays of printed dipoles,” IEEE Trans. Antennas Propagat., vol. 33, pp. 1045–1053, Oct. 1985.

[12] D. M. Pozar, “Finite phased arrays of rectangular microstrip patches,” IEEE Trans. Antennas Propagat., vol. 34, pp. 658–665, May 1986.

[13] C.- C. Liu, A. Hassel, and J. Shmoys, “Performance of probe-fed microstrip-patch element phased arrays,” IEEE Trans. Antennas Propagat., vol. 36, pp. 1501–1509, Nov. 1988.

[14] V. B. Erturk, O. Bakir, R. G. Rojas, and B. Guner, “Scan blindness phenomenon in conformal finite phased arrays of printed dipoles,” IEEE Trans. Antennas Propag., vol. 54, pp. 1699–1708, Jun. 2006.

[15] D. M. Pozar, “Scanning characteristics of infinite arrays of printed antenna subarrays,” IEEE Trans. Antennas Propagat., vol. 40, pp. 666–674, June 1992.

[16] R. B. Waterhouse, “Improving the scan performance of probe-fed microstrip patch arrays on high dielectric constant substrates,” IEEE Trans. Antennas Propagat., vol. 43, pp. 705-712, Jul. 1995.

[17] R. B. Waterhouse, “The use of shorting posts to improve the scanning range of probe-fed microstrip patch phased arrays,” IEEE Trans. Antennas Propag., vol. 44, no. 3, pp. 302–309, Mar. 1996.

[18] W. J. Tsay and D. M. Pozar,“Radiation and scattering from infinite periodic printed antennas with inhomogeneous media,” IEEE Trans. Antennas Propagat., vol. 46, pp. 1641–1650, Nov. 1998.

[19] R. L. Chen, D. R. Jackson, J. T. Williams, and S. A. Long “Scan impedance of RSW microstrip antennas in finite array,” IEEE Trans. Antennas Propagat., vol. 53, pp. 1098-1104, Mar. 2005.

[20] T. Crepin, J. P. Martinaud, T. Dousset, P. Rodriguez-Ulibarri, M. Beruete, C. Loecker, T. Bertuch, J. A. Marcotegui, and S. Maci, "Blind spot mitigation in phased array antenna using metamaterials," IEEE Int. Radar Conf., 2014.

[21] M. C. Tang, S. Xiao, B. Wang, J. Guan, and T. Deng, “Improved performance of a microstrip phased array using broadband and ultralow-loss metamaterial slabs,” ,” IEEE Antennas Propagat. Mag., vol. 53, pp. 31–41, Dec. 2011.

[22] H. Moghadas, A. Tavakoh, and M. Salehi, “Elimination of scan blindness in microstrip scanning array antennas using defected ground structure,” AEU-Int. J. Electron. Commun., vol. 62, pp. 155–158, 2008.

[23] D. B. Hou, S. Xiao, B. Z. Wang, L. Jiang, J. Wang, and W. Hong, “Elimination of scan blindness with compact defected ground structures in microstrip phased array,” IET Microw. Antennas Propag., vol. 3, pp. 269–275, Mar. 2009.

[24] M. H. Awida, A. H. Kamel, and A. E. Fathy, “Analysis and design of wide-scan angle wide-band phased arrays of substrate-integrated cavity backed patches ,” IEEE Trans. Antennas Propag., vol. 61, pp. 3034-3041, Jun. 2013.

[25] P. K. Kelly, L. Diaz, M. Piket-May, and I. Rumsey, “Investigation of scan blindness mitigation using photonic bandgap structure in phased arrays,” in Proc. SPIE, vol. 3464, July 1999, pp. 239–248.

[26] L. Zhang, J. A. Castaneda, and N. G. Alexopoulos, “Scan blindness free phased array design using PBG materials,” IEEE Trans. Antennas Propagat., vol. 52, pp. 2000–2007, August 2004.

[27] Y. Fu and N. Yuan, “Elimination of scan blindness in phased array of microstrip patches using electromagnetic bandgap materials,” IEEE Antennas Wireless Propag. Lett., vol. 3, pp. 63–65, 2004.

[28] G. Donzelli, F. Capolino, S. Boscolo, and M. Midrio, “Elimination of scan blindness in phased array antenna using a grounded-dielectric EBG material,” IEEE Antennas Wireless Propag. Lett., vol. 6, pp. 106–109, 2007.

[29] Z. Iluz, R. Shavit, and R. Bauer, “Microstrip antenna phased array with electromagnetic bandgap substrate,” IEEE Trans. Antennas Propagat., vol. 52, pp. 1446–1453, June 2004.

[30] M. S. M. Isa, R. J. Langley, S. Khamas, A. A. M. Isa, M. Zin, Z. Zakaria, N. Z. Haron, and A. Ahmad, "A technique of scan blindness elimination for planar phased array antenna using miniaturized EBG," Jurnal Teknologi, vol. 69, pp. 11-15, Mar. 2014.

[31] J. E. Jerauld and D. C. Cook, “Electromagnetic Band Gap Structure for Enhanced Scanning Performance in Phased Array Apertures,” U.S. Patent 2014/0028524 A1, published Jul. 26, 2012; issued Jan. 30, 2014.

[32] Y.-Y. Bai, S. Xiao, M.-C. Tang, Z.-F. Ding, and B.-Z. Wang, “Wide-angle scanning phased array with pattern reconfigurable elements,” IEEE Trans. Antennas Propag., vol. 59, no. 11, pp. 4071–4076, Nov. 2011.

[33] R. Wang, B.-Z. Wang, X. Ding, and X.-S. Yang, “Planar phased array with wide-angle scanning performance based on the image theory,” IEEE Antennas Wireless Propag., vol. 63, pp. 3908–3917, Sep. 2015.

[34] S. E. Valavan, D. Tran, A. G. Yarovoy, and A. G. Roederer, “Dual-band wide-angle scanning planar phased array in X/Ku-bands,” IEEE Trans. Antennas Propag., vol. 62, no. 5, pp. 2514–2521, May 2014.

[35] R.-L. Xia, S.-W. Qu, X. Bai, Q. Jiang, S. Yang, and Z.-P. Nie, “Experimental investigation of wide-angle impedance matching of phased array using overlapped feeding network,” IEEE Antennas Wireless Propag., vol. 13, pp. 1284–1287, Jul. 2014.

[36] J. A. Kasemodel, C. C. Chen, and J. L. Volakis, “Wideband planar array with integrated feed and matching network for wide-angle scanning,” IEEE Trans. Antennas Propagat., vol. 61, pp. 4528–4537, Sep. 2013.

[37] M. Li, S. Q. Xiao, and B. Z. Wang, “Investigation of using high impedance surfaces for wide-angle scanning arrays,” IEEE Trans. Antennas Propagat., vol. 63, pp. 2895–2901, July 2015.

[38] F. R. Yang, K. P. Ma, Y. Qian, and T. Itoh, “A novel TEM waveguide using uniplanar compact photonic-bandgap (UC-PBG) structure,” IEEE Trans. Microwave Theory and Techniques, vol. 47, pp. 2092–2098, Nov. 1999.

[39] H. Y. D. Yang, R. Ki, and D. R. Jackson, "Design consideration for modeless integrated circuit substrates using planar periodic patches," IEEE Trans. Microwave Theory and Techniques, vol. 48, pp. 2233–2239, Dec. 2000.

[40] C. A. Kyriazidou, H. F. Contopanagos, and N. G. Alexopoulos, “Space-frequency projection of planar AMCs on integrated for 60 GHz radios,” IEEE Trans. Antennas Propagat., vol. 60, pp. 1899-1909, Apr. 2012.

[41] A. Vallecchi, J. R. De Luis, F. Capolino, and F. De Flaviis, “Low profile fully planar folded dipole antenna on a high impedance surface,” IEEE Trans. Antennas Propagat., vol. 60, pp. 51-62, Jan. 2012.

[42] N. G. Alexopoulos and D. R. Jackson “Fundamental superstrate (cover) effects on printed circuit antennas,” IEEE Trans. Antennas Propag., vol. 32, pp. 807-816, Aug. 1984.

[43] D. F. Sievenpiper, “Forward and backward leaky wave radiation with large effective aperture from an electronically tunable textured surface,” IEEE Trans. Antennas Propagat., vol. 53, no. 1, pp. 236–247, Jan. 2005.

[44] S. Lim, C. Caloz, and T. Itoh, “Metamaterial-based electronically controlled transmission-line structure as a novel leaky-wave antenna with tunable radiation angle and beamwidth,” IEEE Trans. Microw. Theory Tech., vol. 53, no. 1, pp. 161–173, Jan. 2005.

[45] C. Guclu, J. Sloan, S. Pan, and F. Capolino, “Direct use of the high impedance surface as an antenna without dipole on top,” IEEE Antennas Wireless Propag. Lett., vol. 10, pp. 1536–1539, 2011.

[46] W. Liu, Z. N. Chen, and X. Qing, “Metamaterial-based low-profile broadband mushroom antenna,” IEEE Trans. Antennas Propag., vol. 62, pp. 1165–1172, Mar. 2014.

[47] J. Liang and H.-Y. D. Yang, “Radiation characteristics of a microstrip patch over an electromagnetic bandgap surface,” IEEE Trans. Antennas Propag., vol. 55, no. 6, pp. 1691–1697, Jun. 2007.

[48] D. M. Pozar, “The active element pattern,” IEEE Trans. Antennas Propagat., vol. 42, pp. 1176–1178, Aug. 1994.

[49] D. F. Kelley and W. L. Stutzman “Array antenna pattern modeling methods that include mutual coupling effects,” IEEE Trans. Antennas Propagat., vol. 41, pp. 1625–1632, Dec. 1993.